

Removal of Cr(III) Ions from Water Using Magnetically Separable Graphene-Oxide-Decorated Nickel Ferrite Nanoparticles

Jose Luis Ortiz-Quinonez, Francisco Enrique Cancino-Gordillo, and Umapada Pal*

Cite This: <https://doi.org/10.1021/acsnm.3c03618>

Read Online

ACCESS |



Metrics & More



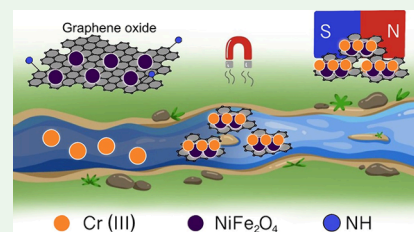
Article Recommendations



Supporting Information

ABSTRACT: Removing toxic metal ions from water is a challenging task due to the increasing demand for potable water worldwide. Utilization of an efficient adsorbent has been the key strategy for addressing this issue. However, the adsorbents utilized so far, whether carbon-based or silica-based, present difficulties in separation from water and pose a harm to aquatic life. In this study, we present a novel approach involving the fabrication of well-dispersed NiFe_2O_4 nanoparticles, averaging approximately 7 nm in size, integrated with graphene oxide. This nanocomposite proves to be highly effective in removing Cr(III) ions from water. At room temperature, it exhibits a superparamagnetic behavior, enabling easy magnetic separation of the adsorbent from the water. By utilizing the nanocomposite, we achieved a removal rate of approximately 17 mg/g for Cr(III) ions dissolved in water. This ensures that their concentration in the water remains below the EPA-prescribed permissible level of 0.1 mg L^{-1} . Additionally, we propose a simple and cost-effective optical method for detecting Cr(III) ions in water. This innovative approach shows great promise in tackling the challenge of toxic metal ion removal from water, offering an efficient and environmentally friendly solution.

KEYWORDS: metal ferrite, nanoparticles, adsorbent, Cr(III) removal, wastewater treatment



1. INTRODUCTION

Cr(III) and Cr(VI) ions are two toxic species frequently present in groundwater, affecting human health severely.¹ As the toxicity of Cr(VI) ions is considerably higher than the toxicity of Cr(III) ions, most research groups have dedicated their efforts for developing strategies to remove Cr(VI) ions from water. However, the relatively less toxic Cr(III) ions can be easily oxidized to Cr(VI) ions in water in the presence of oxidizing agents such as H_2O_2 , MnO_2 , Cl_2 , Ascomycete fungi, $\cdot\text{OH}$ radicals generated by photolysis of $\text{Fe}(\text{OH})^{2+}$, and Fe(III) ion released from minerals such as serpentinite.^{2,3} Therefore, the removal of Cr(III) ions from water remains an essential task.⁴ Cr(III) ions are frequently present in water as $\text{Cr}(\text{H}_2\text{O})_6^{3+}$, $[\text{Cr}(\text{H}_2\text{O})_5(\text{OH})]^{2+}$, $[\text{Cr}(\text{H}_2\text{O})_4(\text{OH})_2]^+$, and other complex species. In the presence of oxidizing species in water, Cr(III) ions are oxidized to Cr(VI) ions, forming species such as CrO_4^{2-} and $\text{Cr}_2\text{O}_7^{2-}$. Very often, these CrO_4^{2-} and $\text{Cr}_2\text{O}_7^{2-}$ ions are present in wastewater emanating from industries such as tanning, metal finishing, electroplating, and dye manufacturing.^{5,6} Major sources of Cr(VI) in drinking water are discharges from steel and pulp industries, metal plating factories, and the erosion of natural deposits of trivalent chromium.⁷ Some industries generate wastewater containing complexes of Cr(III) ions with ligands such as ethylenediaminetetraacetic acid (EDTA), citric acid, tartaric acid, and nitrilotriacetic acid.^{6,8} Cr(VI) ions in the form of CrO_4^{2-} and $\text{Cr}_2\text{O}_7^{2-}$ are considered cancerogenic and toxic to human health and reported to cause brain cancer, anemia, lung cancer, severe dermatitis, digestive tract damage, DNA damage,

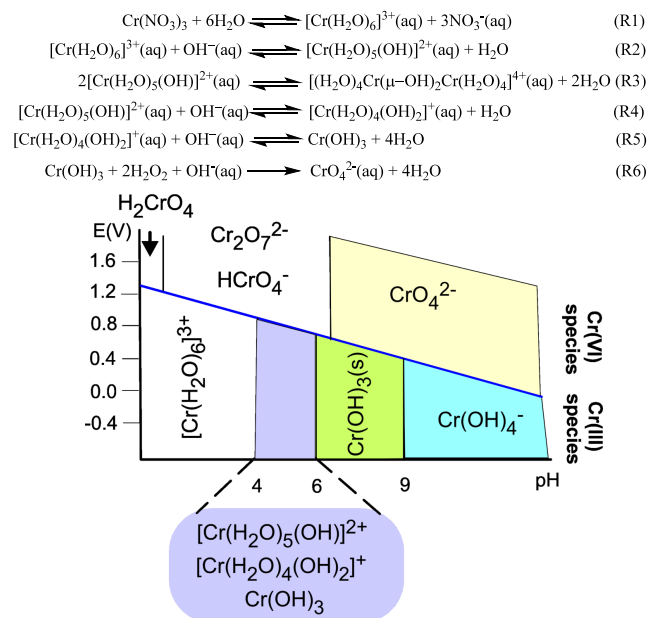
tubular alteration at the renal level, kidney failure, and several other health ailments.^{7,9} The EPA's (Environmental Protection Agency's) regulation for total chromium (Cr(III) and/or Cr(VI)) ions allowed in drinking water is 0.1 mg L^{-1} or 0.1 ppm.¹ Therefore, removing these toxic ions from water is essential not only for humans but also for other aquatic and nonaquatic living organisms.

Some important reactions associated with Cr(III) and Cr(VI) ionic species are presented in reactions R1–R6. Once a chromium salt is dissolved in water, $[\text{Cr}(\text{H}_2\text{O})_6]^{3+}$ ions are generated (reaction R1). As this ion has a $\text{p}K_a$ as low as 4,¹⁰ some of the H_2O molecules bonded to the Cr(III) ions get hydrolyzed at pH higher than 4 to generate several metal-hydroxide complexes. For example, the $[\text{Cr}(\text{H}_2\text{O})_5(\text{OH})]^{2+}$ species is generated through reaction R2, which could further react to generate chromium hydroxide ions as shown in reactions R3 and R4.¹⁰ At pH values of 6 or higher, $\text{Cr}(\text{OH})_3$ species are also generated through reaction R5. As typical pH values for *subterranean water*, drinking water, or wastewater remain between 5.5 and 7, $[\text{Cr}(\text{H}_2\text{O})_5(\text{OH})]^{2+}$, $[\text{Cr}(\text{H}_2\text{O})_4(\text{OH})_2]^+$, and $\text{Cr}(\text{OH})_3$ are the most abundant chromium species in them (Scheme 1). Therefore, we need

Received: August 24, 2023

Accepted: September 4, 2023

Scheme 1. (Top) Selective Chemical Reactions Involving Cr(III) Ion in Aqueous Solution. (Bottom) Chromium Species Present in Water as a Function of pH and Potential (Electrode Potential or Oxidation-Reduction Potential). Adapted from N. Unceta et al., *Anal. Bioanal. Chem.* (2010) 397:1097–1111. Copyright (2010) Springer Nature^{9a}



^aThe scheme indicates which species is predominant at certain values of pH and potential. The zone below the blue line corresponds to the couples of pH and potential values for which the Cr(III) species are predominant. At high pH values, the Cr(III) ions easily get oxidized to Cr(VI) ions in the presence of oxidants.

efficient adsorbents for removing these species from potable water. In fact, several metal oxides, clays, zeolites, and carbon-based adsorbents have been utilized to remove chromium salt ions from water.^{8,11–15}

Several nanostructures and nanocomposites have been used as adsorbents of chromium ions. Adsorbent materials frequently used for the removal of Cr(III) ions from water include mesoporous SBA-15 functionalized with 2-acetylthiophene¹³ and sodium titanate ($\text{Na}_2\text{Ti}_3\text{O}_7$) nanotubes functionalized with citric acid, humic acid, or fulvic acid.¹⁶ On the other hand, ferrihydrite was evaluated by Zhang et al. for the adsorption of Cr(III)-EDTA complexes.⁶ In the case of hexavalent chromium ion (Cr(VI)), the frequently used adsorbent materials are polydopamine microspheres, metal organic frameworks,¹⁷ reduced graphene oxide/polyethylenimine nanocomposite,¹⁸ Mn-incorporated ferrihydrite,⁵ graphene oxide/chitosan-based aerogel,¹⁹ composites based on NiFe layered double hydroxides (LDH), and 3D hierarchical graphene oxides.²⁰ However, only a few studies have reported the adsorption of both Cr(III) and Cr(VI) ions using a single adsorbent. For example, sodium titanate nanotubes and $\text{MoS}_2@\text{Fe}_3\text{O}_4$ nanoparticles have been used to remove Cr(III) and Cr(VI) ions from deionized (DI) water at different pH.^{21,22}

Metal ferrites and metal-ferrite-based composites have been used for the removal of several toxic ions from drinking water. For example, cobalt ferrite nanoparticle-decorated faujasite zeolite has been used for the removal of Pb^{2+} ions.²³ The nanocomposite could adsorb Pb^{2+} ions from water with an

adsorption capacity as high as 602.4 mg g^{-1} . $\text{Mn}_{0.2}\text{Fe}_{2.8}\text{O}_4$ NPs functionalized with different ligands (phthalic anhydride, succinic anhydride, acetic anhydride, 3-phosphonopropionic acid, and 16-phosphonohexadecanoic acid) have been used for simultaneous removal of Pb^{2+} , Cd^{2+} , and Cu^{2+} ions from apple (pH = 2.07), tomato (pH = 4.98), and potato juices (pH = 6.20).²⁴ It was found that the pH of the liquid samples and the ligand used affect the adsorption capacity of the NPs considerably. However, the nickel ferrite (NiFe_2O_4) nanoparticles or their carbonaceous composites, which possess considerable ferrimagnetic behavior and hence can be easily separated from aqueous solutions magnetically, have not been evaluated as adsorbent materials for the removal of Cr(III) ions from water. Graphene oxide has several advantages when used in nanocomposites for removal of toxic ions from water. The advantages include its high surface area, good dispersibility in many solvents (include water), and presence of functional groups such as carboxylic acid ($-\text{COOH}$), ketone ($-\text{C}=\text{O}$), and alcohol/phenol ($-\text{C}-\text{OH}$), which facilitate the absorption of toxic ions.^{25,26} Moreover, the electrostatic interaction between these functional groups and the nanoparticles grown on GO reduces the agglomeration of the ferro- and ferrimagnetic nanoparticles.²⁷

Another important issue in the removal of chromium ions from water is the quantification of its concentration. After removing the adsorbent materials, $[\text{Cr(H}_2\text{O)}_5(\text{OH})]^{2+}$, $[\text{Cr(H}_2\text{O)}_4(\text{OH})_2]^{+}$, and other chromium-based ions remain in the water. However, the concentration of these ions cannot be determined by UV–visible spectrometry, as these ions do not absorb electromagnetic radiation in this spectral range. A solution to this problem might be to increase the pH of the aqueous solution to generate Cr(OH)_3 and Cr(OH)_4^- anions (the region with turquoise color in Scheme 1) and then add H_2O_2 to progressively oxidize these two species to CrO_4^{2-} (the region with pale yellow color in Scheme 1). As CrO_4^{2-} ion absorbs electromagnetic radiation in the UV–visible range, the aforementioned quantification problem can be addressed by transforming Cr(III) ions to CrO_4^{2-} ions by H_2O_2 treatment. Reaction R6 depicts an example of this oxidation (from Cr(III) to Cr(VI)) process.

In this work, we report the synthesis of NiFe_2O_4 nanoparticles (NPs) and $\text{NiFe}_2\text{O}_4/\text{GO}$ nanocomposite by a hydrothermal process assisted by NH_4OH . Small (4–9 nm) NiFe_2O_4 nanoparticles well-dispersed over graphene oxide layers could be synthesized. X-ray photoelectron spectroscopy revealed a strong metal–support interaction (MSI) between the NPs and the GO sheets. Moreover, graphene oxide was seen to be functionalized with NH_2 groups during hydrothermal treatment in the presence of NH_4OH . Both the NiFe_2O_4 NPs and $\text{NiFe}_2\text{O}_4/\text{GO}$ nanocomposite manifested their high capacity for removing Cr(III) ions from water. The $\text{NiFe}_2\text{O}_4/\text{GO}$ nanocomposite exhibited a Cr(III) ion capture performance superior to that of the bare NiFe_2O_4 nanoparticles.

2. EXPERIMENTAL SECTION

2.1. Materials and Methods. The reagents used for the synthesis of nickel ferrite nanostructures were nickel chloride hexahydrate ($\text{NiCl}_2 \cdot 6\text{H}_2\text{O}$, Fermont, 99%), iron chloride hexahydrate ($\text{FeCl}_3 \cdot 6\text{H}_2\text{O}$, Sigma, 97%), ethylene glycol ($\text{HOCH}_2\text{CH}_2\text{OH}$, J.T. Baker, 99.75%), ammonium hydroxide (NH_4OH , CTR, 29.5%), sodium acetate anhydrous (CH_3COONa , J.T. Baker, 99.9%) polyvinylpyrrolidone (PVP, $\text{C}_6\text{H}_9\text{NO}$, number-average molecular weight (Mn): 360,

Sigma-Aldrich), potassium permanganate (KMnO_4 , Sigma-Aldrich, 99%) sulfuric acid (H_2SO_4 , Fermont, 99%), phosphoric acid (H_3PO_4 , Fermont, 85.4%), and hydrogen peroxide (H_2O_2 , Merck, 30%). Chromium nitrate ($\text{Cr}(\text{NO}_3)_3 \cdot 9\text{H}_2\text{O}$, Sigma, 99%) and sodium hydroxide (NaOH , J.T. Baker, 98.15%) were utilized to prepare Cr(III) ion solution and adjust its pH. Deionized water from the Millipore water purification system ($\rho > 18.2 \text{ M}\Omega\text{-cm}$), ethanol (CTR Scientific, Mexico, 99.9%), and methanol (J. T. Baker, 99.9%) were utilized for preparing the samples and washing the nanostructures.

Powder X-ray diffraction (XRD) patterns of the samples were recorded in a Panalytical-Empyrean diffractometer, providing monochromatic $\text{Cu K}\alpha$ emission ($\lambda = 1.5406 \text{ \AA}$) as the excitation radiation. Raman spectra of the samples were recorded in a LabRAM-HR spectrometer (HORIBA-Jobin Yvon) equipped with a He-Ne laser ($\lambda = 632.8 \text{ nm}$) and a thermoelectrically cooled charged couple device (CCD) detector. FTIR spectra were recorded in a PerkinElmer spectrometer (Spectrum GX FT-IR) using well-dried KBr to form thin pellets of the samples (98:2 ratio of KBr and sample). A JEOL JSM-7800F field-emission scanning electron microscope (SEM) operating at 3.0 kV was utilized for analyzing the morphology and dispersion of NiFe_2O_4 NPs over GO. Transmission electron microscopy (TEM) and high-resolution transmission electron microscopy (HRTEM) images of the samples were recorded in a JEOL 2010F microscope. For SEM analysis, the powder samples were ultrasonically dispersed in ethanol, and then a drop of the dispersion was deposited onto a silicon substrate. For TEM and HRTEM analysis, the samples were prepared by spreading a drop of ethanolic dispersion of the nanostructures over carbon-coated Cu grids and subsequent drying at room temperature. Magnetization curves and zero field cooling (ZFC) and field cooling (FC) curves of the nanostructures were recorded in a physical property measurement system (PPMS, DynaCool-9). An X-ray photoelectron spectrometer (XPS, Thermo Scientific) with an $\text{Al K}\alpha$ (1486.6 eV) radiation source was utilized to analyze the surface composition of the nanostructures. The surface area of the nanoparticles and nanocomposites was analyzed from their N_2 adsorption-desorption curves recorded at 77 K in a Belsorp-II (BEL, Japan Inc.) sorptometer. Before the adsorption-desorption isotherms were recorded, the samples were degasified at 90 °C for 16 h under a vacuum ($\sim 10^{-3}$ Torr). Zeta potentials of the samples were measured in a Zeta potential analyzer (Malvern Panalytical) at 25 °C in water at pH 6.5. Adsorption of Cr(III) ions dissolved in water over the NiFe_2O_4 nanoparticles and $\text{NiFe}_2\text{O}_4/\text{GO}$ nanocomposite was monitored with a UV-vis-NIR spectrophotometer (Shimadzu UV-3101PC) at room temperature.

2.2. Synthesis of Graphene Oxide. Graphene oxide was synthesized by a modified Tour method.²⁸ In brief, 40 mL of H_3PO_4 was added slowly to 360 mL of H_2SO_4 in a 500 mL glass beaker. Separately, 3 g of graphite flake was mixed with 18 g of KMnO_4 . The mixture was then added slowly to the $\text{H}_3\text{PO}_4/\text{H}_2\text{SO}_4$ solution and heated to 50 °C for 17 h under magnetic stirring. The obtained purple-brown mixture was then transferred to a beaker containing ice cubes prepared by freezing 400 mL of DI water. After 8 h under magnetic stirring, 10 mL of H_2O_2 was added to the mixture, resulting in a yellow suspension. The suspended solid was washed with 800 mL of a dilute HCl solution ($\text{HCl}/\text{H}_2\text{O}$ 1:9) and separated by centrifugation (5000 rpm for 1 h). After that, the solid was washed first with 500 mL of a DI water/ethanol (8:2) mixture and then with DI water until the pH of the supernatant became ~ 3.5 . In all the washing steps, the suspension was centrifuged at 5000 rpm for 30 min. The product was then dried under a vacuum for 96 h. The obtained solid (~ 4.3 g) was grounded in a mortar and stored for further utilization.

2.3. Synthesis of NiFe_2O_4 NPs. In a typical synthesis process of NiFe_2O_4 NPs, 12 mmol (3.2423 g) of $\text{FeCl}_3 \cdot 6\text{H}_2\text{O}$, 6 mmol (1.4255 g) of $\text{NiCl}_2 \cdot 6\text{H}_2\text{O}$, 18 mmol (1.4765 g) of CH_3COONa , and 1.333 g of PVP were mixed with 84 mL of ethylene glycol under magnetic stirring. The mixture was heated at 70 °C for 60 min under magnetic stirring to dissolve all the reagents. After that, the solution was cooled down to room temperature, and about 36 mL of NH_4OH was slowly added to adjust the pH to approximately 12. The mixture was

immediately transferred to four 30 mL Teflon vessels, which were sealed with Teflon caps and placed inside stainless-steel autoclaves. The autoclaves were heated at 190 °C for 36 h inside a gravity furnace (Lindberg Blue). After cooling down to room temperature, the obtained solid was separated by centrifugation at 7000 rpm for 30 min and washed with ethanol, then with methanol, and finally with water (three times with each solvent) sequentially to remove the PVP and byproducts such as CH_3COONa , NaCl , NH_4Cl , and $[\text{Ni}(\text{NH}_3)_6]\text{Cl}_2$, along with the unreacted precursors. Finally, the product was dried at 60 °C for 6 h. The dried product was ground in an Agata mortar (obtaining about 2.0 g of powder) and stored for further use.

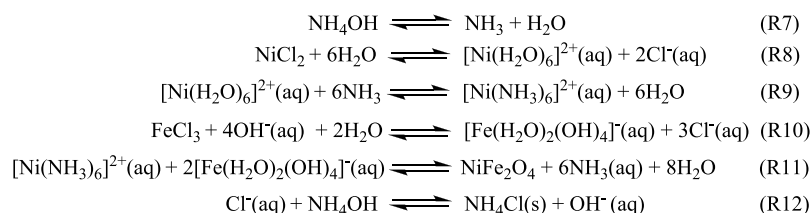
2.4. Synthesis of NiFe_2O_4 NPs over Graphene Oxide. In a typical procedure, 0.615 g of graphene oxide was added to 10 mL of ethylene glycol and left for soaking for 24 h. The wet graphene oxide was then ground in an Agata mortar to promote its exfoliation. The obtained suspension was mixed with 74 mL of ethylene glycol. After that, the procedure described in Section 2.3 was followed to synthesize the $\text{NiFe}_2\text{O}_4/\text{GO}$ nanocomposite. The amount of graphene oxide used in the synthesis was selected to maintain a nominal 30 wt % of graphene oxide in the nanocomposite. During washing of the product obtained in the hydrothermal reaction, the unsupported graphene oxide is removed, and hence, the real graphene oxide content in the final sample probably is a bit lower than its nominal content, i.e., 30 wt %. It is worth mentioning that the thermal treatment in ethylene glycol partially reduces the graphene oxide, as ethylene glycol at high temperatures (for example, 160 °C) reduces the epoxy groups in graphene oxide.²⁹

2.5. Calibration Curves for Quantifying the Cr(III) Ions Present in Water. Considering Scheme 1, the oxidation of Cr(III) to Cr(VI) to generate CrO_4^{2-} ions requires oxidizing conditions (e.g., adding species such as H_2O_2) and basic environments ($\text{pH} > 7$). On the other hand, the formation of Cr(VI) ions in water can be monitored by measuring the optical absorption of the CrO_4^{2-} ions, which exhibit an absorption band centered around 373 nm in the UV-vis spectrum. To optimize the experimental conditions for oxidizing Cr(III) to Cr(VI), we prepared a solution of 10 ppm of Cr(III) and took several aliquots of 10 mL. The pH of the aliquots was adjusted to different pH values (> 7), and 50 μL of H_2O_2 was added. The aliquots were left under magnetic stirring for 60 min, and their UV-vis spectra were recorded. It was found that at pH 11.3, the absorbance at 373 nm is the highest. Higher pH values or larger volumes of H_2O_2 did not increase the absorbance at 373 nm.

Before performing the Cr(III) ion adsorption tests of the fabricated nanostructures, first an aqueous solution of Cr(III) ions of 1000 ppm concentration was prepared by dissolving 192.4 mg of $\text{Cr}(\text{NO}_3)_3 \cdot 9\text{H}_2\text{O}$ in 25 mL of DI water. The solution was light blue. Then Cr(III) ion solutions of 0.5, 1.0, 2.5, 5, 10, 15, and 20 ppm were prepared by diluting the earlier solution to prepare a calibration curve. Three milliliters of each of the latter solutions was taken in 10 mL glass vials, and approximately 0.5 mL of 0.02 M NaOH solution was added into them under vigorous magnetic stirring to adjust their pH to 11.3. After 10 min of magnetic agitation, 50 μL of H_2O_2 solution (30%) was added into each of the vials, and the magnetic stirring was continued for a further 60 min. Finally, the UV-visible absorption spectra of the solutions were recorded in a Shimadzu 3101PC double-beam spectrophotometer.

2.6. Removal of Cr(III) Ions Dissolved in Water. To perform the Cr(III) adsorption tests, 100 mL of a 10 ppm solution of Cr(III) ions was taken into a glass beaker. Then, 50 mg of the metal ferrite NPs or nanocomposite was added to the solution and left under mechanical stirring. Aliquots of about 10 mL were taken out of the mixture solution with a plastic syringe at 0, 10, 20, 30, 60, 90, and 120 min intervals, and the adsorbents were separated by an NdFeB magnet. All of the aliquots were then centrifuged at 7500 rpm for 4 min to precipitate the smaller nanoparticles. After that, each of the obtained solutions was filtered by a nitrocellulose membrane (0.22 μm pore size). The pH of the aliquots was adjusted to 11.3 by adding approximately 1.5 mL of a 0.02 M NaOH solution, and then 50 μL of the H_2O_2 solution was added to oxidize the Cr(III) species to CrO_4^{2-} ions. Finally, the solutions were magnetically stirred for 60 min, and

Scheme 2. (Top) Proposed Chemical Reactions Involved in the Formation of NiFe₂O₄ NPs in the Presence of Ammonia Hydroxide. (Bottom) Logarithm of the Stability Constants (*K*'s) Reported for Ni²⁺ and Fe³⁺ Cations Bonded to NH₃ or OH⁻ Ligands at 25 °C³⁰



Specie	[Ni(NH ₃) ₆] ²⁺	Ni(OH) ₂	[Fe(H ₂ O) ₂ (OH) ₄] ⁻	[Fe(H ₂ O) ₄ (OH) ₂] ⁺	NH ₄ ⁺
log <i>K</i>	9.04 ± 0.04	8	34.4	21.9	9.4

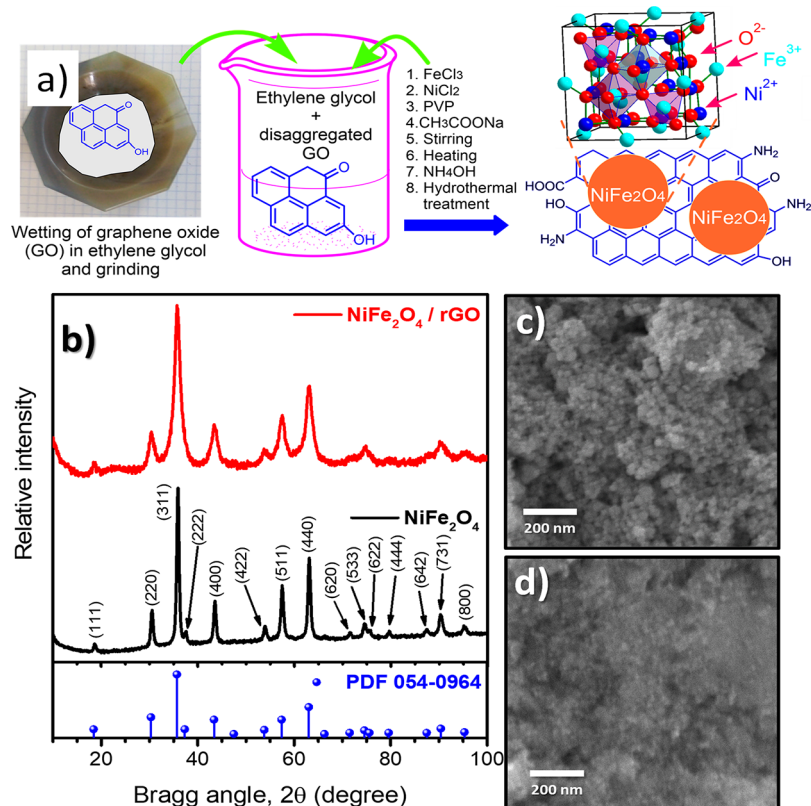


Figure 1. (a) Schematic of the synthesis process adopted for obtaining NiFe₂O₄/GO nanocomposite and its crystal structure. (b) XRD patterns of bare and GO-supported nickel ferrite nanoparticles. (c, d) Typical SEM images of (c) bare and (d) GO-supported nickel ferrite nanoparticles.

their UV–vis absorption spectra were recorded at room temperature to monitor the concentration of residual Cr(III) ions in the solution.

2.7. Reusability Test of the Nanocomposite Adsorbent. The reusability tests of the NiFe₂O₄/GO nanocomposite for adsorbing Cr(III) ions were performed by recovering the adsorbent from its previous adsorption tests. The tests were performed for both the unactivated and activated adsorbents. In the earlier case, the adsorbent collected by magnetic separation after its first adsorption test was washed with fresh deionized water, dried at 50 °C, and reutilized for the subsequent test. For the latter case, the NiFe₂O₄/GO nanocomposite collected after the first adsorption test was washed with DI water and then activated by mixing with 25 mL of 1 M NaOH aqueous solution for 30 min. After that, the adsorbent was washed with DI water two times and dried at 50 °C. Reusability tests were performed for four cycles for each of the cases.

3. RESULTS AND DISCUSSION

3.1. Material Synthesis. NiFe₂O₄ nanoparticles were initially synthesized without adding NH₄OH and adding 8 mL of NH₄OH to the reaction mixture. However, the reaction yields were considerably low, and several unidentified by-products were formed along with the metal ferrite. Hence, for the synthesis of the nanoparticles and nanocomposites in the pure phase, the volume of NH₄OH solution was increased to 36 mL to increase the OH⁻ ion concentration in the reaction mixture. Although Ni(OH)₂ solid could be formed during the synthesis of NiFe₂O₄ at the used reaction conditions, it gets dissolved in NH₃ of the reaction mixture to generate [Ni(NH₃)₆]²⁺, as has been reported by Housecroft and Sharpe.¹⁰ Consequently, the dominant nickel species in the mixture under the reaction conditions is [Ni(NH₃)₆]²⁺. The

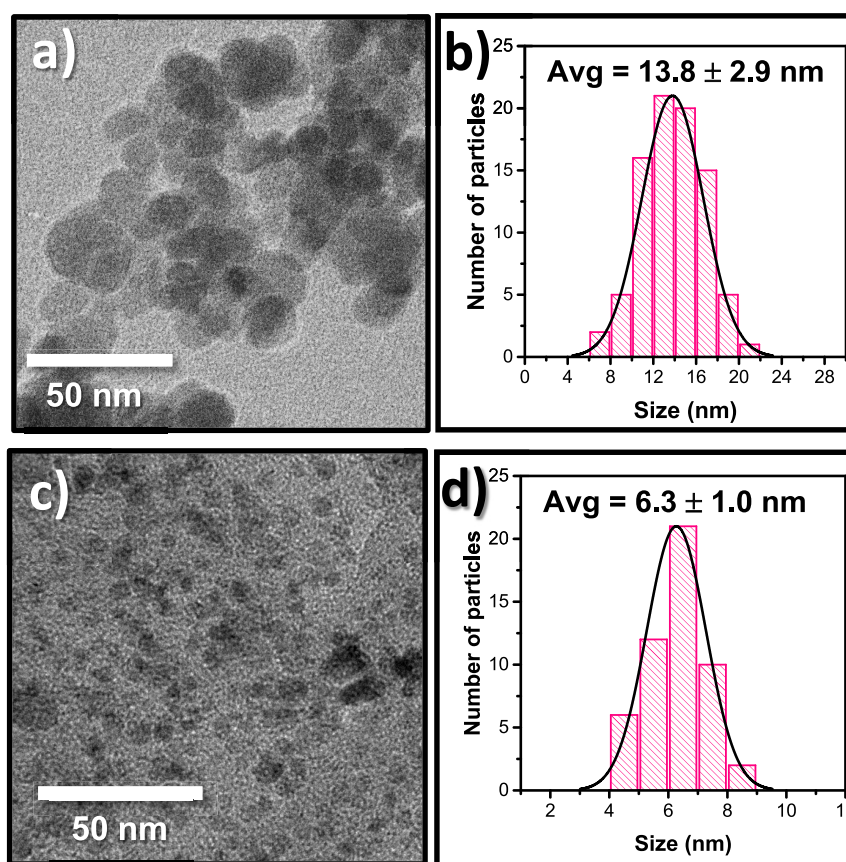


Figure 2. Typical TEM images of nickel ferrite nanoparticles and their nanocomposites with GO, along with their size distribution histograms: (a, b) NiFe_2O_4 and (c, d) $\text{NiFe}_2\text{O}_4/\text{GO}$.

reactions leading to the formation of $[\text{Ni}(\text{NH}_3)_6]^{2+}$ are presented in reactions R7–R9 (Scheme 2). The reaction leading to the formation of the $[\text{Fe}(\text{H}_2\text{O})_2(\text{OH})_4]^-$ complex is presented in reaction R10. Under the used high concentration of NH_4OH (and also high temperature) in the reaction mixture, $[\text{Fe}(\text{H}_2\text{O})_2(\text{OH})_4]^-$ is formed following the reaction presented in reaction R10. This iron hydroxide reacts with the $[\text{Ni}(\text{NH}_3)_6]^{2+}$ complex at high temperatures (reaction R11) to form nickel ferrite. Solid NH_4Cl is also formed as a byproduct (reaction R12). The stability constants (K 's) for some of the above-mentioned reaction products at 25 °C have been reported and are presented at the bottom of Scheme 2.³⁰ The larger the $\log K$ value is, the more stable is the species.

3.2. XRD Analysis. Powder XRD diffraction patterns of the NiFe_2O_4 NPs and $\text{NiFe}_2\text{O}_4/\text{GO}$ nanocomposite are presented in Figure 1b. It can be observed that the position and intensity of the XRD peaks for the NiFe_2O_4 NPs coincide with the standard peak positions of NiFe_2O_4 (PDF # 054-0964) in the spinel structure. The estimated cell parameter for the NPs is $a = b = c = 8.31 \text{ \AA}$. The average crystallite size of the NiFe_2O_4 NPs obtained from Rietveld refinement of the XRD pattern was $13.01 \pm 1.5 \text{ nm}$. On the other hand, although the same diffraction peaks appeared for the $\text{NiFe}_2\text{O}_4/\text{GO}$ nanocomposite, the full width at half-maximum (fwhm) of the diffraction peaks of the NiFe_2O_4 NPs grown over GO is considerably broader than that of the bare NiFe_2O_4 NPs, and the average crystallite size estimated using Rietveld refinement of its XRD pattern is about $5.27 \pm 0.7 \text{ nm}$. The estimated cell parameter of the NiFe_2O_4 nanocrystals grown over GO was $a = b = c = 8.32 \text{ \AA}$. The XRD results confirm that no secondary

phases were present in the NiFe_2O_4 or $\text{NiFe}_2\text{O}_4/\text{GO}$ samples. The XRD results also confirm that the presence of GO affects the nucleation and growth behaviors of the NiFe_2O_4 NPs, as the size of the NPs grown over GO is considerably smaller than that of the bare grown NPs. The presence of $[\text{Ni}(\text{NH}_3)_6]\text{Cl}_2$ and NH_4Cl salts was also detected in the XRD pattern of the samples before washing them with methanol or water (Figure S1, Supporting Information), as it is only sparingly soluble in acetone and only slightly soluble in ethanol (4 g/100 g of solvent). In the case of the synthesis of $\text{NiFe}_2\text{O}_4/\text{GO}$, the species $[\text{Ni}(\text{NH}_3)_6]\text{Cl}_2$, NH_4Cl , and $(\text{NH}_4)_2[\text{NiCl}_4(\text{H}_2\text{O})(\text{NH}_3)]$ were detected in the XRD pattern before washing the sample with water and methanol (Figure S2, Supporting Information). The structure of the $(\text{NH}_4)_2[\text{NiCl}_4(\text{H}_2\text{O})(\text{NH}_3)]$ phase was previously reported by Breternitz.³¹

The relative intensity of the XRD peaks of NiFe_2O_4 NPs indicates that preferential growth did not occur in the nanostructures, and the NPs synthesized using ethylene glycol (EG), PVP, and sodium acetate are of spherical shape. Previous studies carried out for the synthesis of other metal ferrites using EG, PVP, and sodium acetate in the reaction mixture also generated NPs with a spherical shape.³² On the other hand, experimental results confirm that the pH of the solution is a critical parameter for obtaining NiFe_2O_4 NPs in the pure phase with high yields.

3.3. Scanning Electron Microscopy (SEM) and Energy Dispersive Spectroscopy (EDS) Analysis. The composition and morphology of the nickel ferrite nanoparticles and nanocomposite were analyzed in FE-SEM. From the EDS

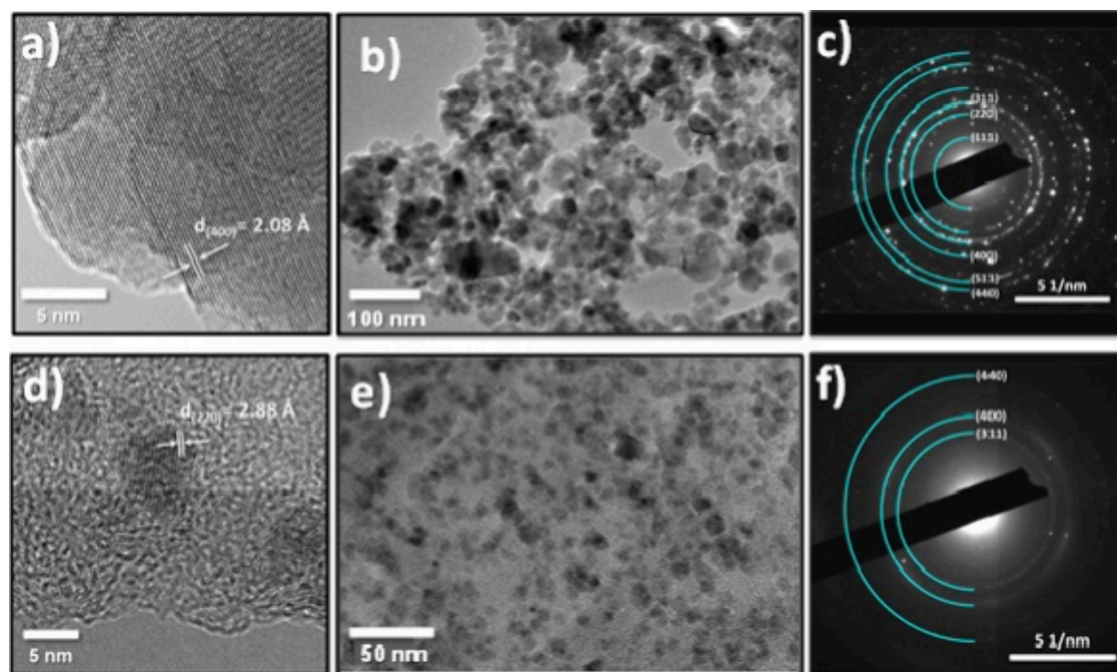


Figure 3. High-resolution transmission electron microscopy (HRTEM) images of (a) bare and (d) GO-supported nickel ferrite nanoparticles. The selected area electron diffraction (SAED) pattern of the bare NiFe_2O_4 NPs shown in panel b is presented in panel c. The SAED pattern of the GO-supported NiFe_2O_4 NPs shown in panel e is presented in panel f.

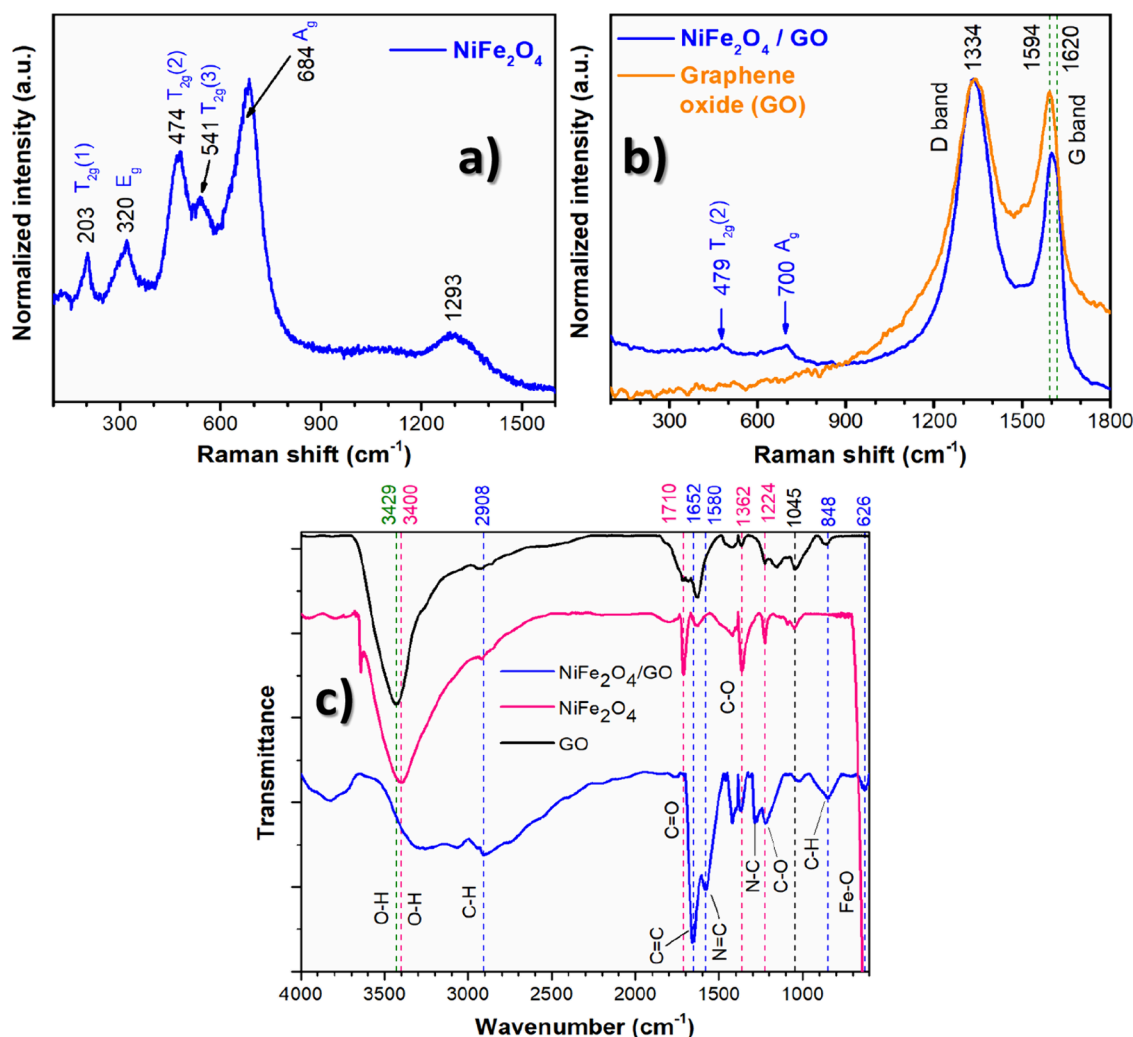
spectra presented in Figure S3 (Supporting Information), it can be seen that sodium or chloride ions are not present in the samples. It can also be noted that some emission peaks of the NiFe_2O_4 nanostructures attributed to the Fe element overlap with Ni emissions. The C/O atomic ratio in the sample containing GO is considerably higher than that in the pure NiFe_2O_4 samples, which confirms the presence of the GO in the nanocomposite. The elemental compositions of the samples estimated from their EDS analysis are presented in Table S1 (Supporting Information). The carbon detected in the bare NPs can be attributed to the adventitious carbon adsorbed at their surface and the carbon bonded at the surface of the nanoparticles during their synthesis.³³ The ideal Fe/Ni atomic ratio in NiFe_2O_4 should be 2.0. However, the value obtained from EDS analysis (Table S1, Supporting Information) of the nanocomposite is higher because a part of the X-rays emitted from Ni atoms is absorbed by the iron atoms present in the sample. The EDS estimated stoichiometry of the pure NiFe_2O_4 NPs and $\text{NiFe}_2\text{O}_4/\text{GO}$ nanocomposite (without considering the contribution of C) indicates that the atomic percentage of the oxygen in pure NiFe_2O_4 NPs is higher than its expected value for an ideal NiFe_2O_4 phase. This discrepancy is attributed to the presence of oxygen atoms forming $\text{Ni}(\text{OH})_x$ groups at the surface of the NPs instead of Ni–O–Fe moieties. As the OH^- species can form only one chemical bond with Ni, a large number of OH^- groups remain present at the surface of NiFe_2O_4 NPs to satisfy the valence of the Fe^{3+} and Ni^{2+} cations at the surface of the NPs. On the other hand, it can be seen from Table S1 (Supporting Information) that the atomic percentage of carbon is about 44.6 for the $\text{NiFe}_2\text{O}_4/\text{GO}$ nanocomposite. That carbon is attributed mainly to the GO, which was partially reduced by the hot ethylene glycol during thermal treatment. Residual carbon due to the presence adventitious carbon also contributes to the estimated atomic percentage of carbon.

Typical SEM images of the bare NiFe_2O_4 NPs and $\text{NiFe}_2\text{O}_4/\text{GO}$ nanocomposite samples are presented in Figures 1c,d, respectively. In Figure S4 (Supporting Information), magnified images of the same are presented for better visualization of the difference between the morphologies of spherical shape in both the samples. Formation of nanometric particles of spherical shape in both the samples is clear in the images. As can be noticed, the size of the nanoparticles formed in both the samples is smaller than 20 nm, which is in well accordance with the crystallite size estimated from their XRD analysis. SEM images of the NiFe_2O_4 NPs grown over graphene oxide (Figure 1d) revealed the formation of even smaller spherical NPs. The smaller size of the NPs grown over GO is probably due to the presence of functional groups such as ketone, aldehyde, epoxide, carboxylate, and phenol on graphene oxide, which work as nucleation centers for the NPs and also hold them apart, avoiding their growth through Ostwald ripening. Moreover, the NH_2 groups formed over the graphene oxide contribute both as nucleation centers and as deaggregating agents, keeping the NPs apart.

3.4. Transmission Electron Microscopy (TEM) Analysis. The morphology and structure of the metal ferrite NPs and nanocomposite were analyzed further by TEM and HRTEM analysis. Typical TEM images of the bare and GO supported NiFe_2O_4 nanoparticles are presented in Figure 2a,c, respectively. As can be noticed, the unsupported particles (Figure 2a) have a spherical shape, with an average size of about $13.8 \pm 2.9 \text{ nm}$ (Figure 2b). On the other hand, when they were grown over GO sheets (Figure 2c), although they maintain the spherical shape, their average size decreased to $6.3 \pm 3.2 \text{ nm}$ (Figure 2d). From the TEM analysis, it is clear that the nickel ferrite nanostructures grown over GO are better dispersed and smaller in size in comparison to the case when they were grown without any support (bare-grown). It is worth mentioning that the NiFe_2O_4 NPs formed over GO are well

Table 1. Selected Works Highlighting the Effect of Using an SDA on the Average Size of CoFe_2O_4 and NiFe_2O_4 NPs Prepared by Solvothermal and Precipitation Methods

phase	method	surface directing agent (SDA)	solvent	shape of the NPs	average size (nm)	ref.
CoFe_2O_4	sonochemical	PVP	water	spherical	10.9 ± 0.9	44
CoFe_2O_4	microwave- assisted solvothermal	acetylacetonate	ethanol		9.8 ± 0.9	45
CoFe_2O_4	thermal decomposition	acetylacetonate Triton-X100	benzyl ether	spherical	5.5 ± 1.2	46
CoFe_2O_4	thermal decomposition	acetylacetonate, oleic acid, oleylamine	benzyl ether	cubic	9.0	47
CoFe_2O_4	thermal decomposition	acetylacetonate, oleic acid, oleylamine	benzyl ether	cubic	28	48
NiFe_2O_4	thermal decomposition	acetylacetonate	1-phenylethanol	spherical	11.4 ± 0.2	49
NiFe_2O_4	hydrothermal	NH_4OH	benzyl alcohol	quasi-spherical	11.3	36

**Figure 4.** Raman spectra of (a) NiFe_2O_4 nanoparticles and (b) NiFe_2O_4 nanoparticles grown over graphene oxide recorded using a 633 nm laser beam. (c) FTIR spectra of GO, NiFe_2O_4 , and $\text{NiFe}_2\text{O}_4/\text{GO}$ samples.

dispersed (neither fused nor agglomerated) possibly because of the lower temperature used ($190\text{ }^\circ\text{C}$) for the hydrothermal treatment and strong metal support interaction between the metal ferrite clusters formed at the initial stage and the GO support. However, as can be noticed in the TEM image of Figure 2, although the bare-grown NiFe_2O_4 NPs are agglomerated to some extent, they are not fused among themselves.

High-resolution TEM (HRTEM) images of the nanostructures presented in Figure 3 reveal the small size and good crystallinity of the nickel ferrite nanoparticles. The HRTEM images of the NiFe_2O_4 nanoparticles (Figure 3a) revealed the

presence of small particles and well-resolved atomic planes, with an interplanar distance of 2.08 \AA , attributed to the (400) plane of NiFe_2O_4 in the spinel structure. On the other hand, the NiFe_2O_4 NPs grown over GO (Figure 3d) also revealed their high crystallinity with well-resolved atomic planes. The average interplanar distance revealed for the (220) plane was about 2.88 \AA , confirming the formation of nickel ferrite NPs. A selected area electron diffraction (SAED) pattern of NiFe_2O_4 NPs taken over the whole area of Figure 3b is shown in Figure 3c. The radii of the rings correspond to the (111), (220), (311), (400), (511), and (440) planes, which confirm the purity of the nickel ferrite NPs. The SAED pattern of the

NiFe₂O₄/GO sample taken over the area covered in Figure 3e is presented in Figure 3f. The radii of the rings are associated with the (311), (400), and (440) planes, confirming the formation of the NiFe₂O₄ in the nanocomposite.

Several methods have been reported for synthesizing NiFe₂O₄ NPs without using any surface directing agent (SDA) such as polymers (e.g., PVP), surfactants (e.g., cetyltrimethylammonium bromide (CTAB)), or ligands (e.g., acetylacetonate (acac)). However, the NPs produced under these synthesis conditions have average sizes larger than 20 nm, and frequently, they are highly agglomerated.³⁴ Large-size or agglomerated NPs are not convenient for applications such as removal of toxic ions from water, etc., where nanomaterials with a high surface area are required. In contrast, when PVP, acac, CTAB, or other species are used as SDA, small-size NiFe₂O₄ NPs with controlled shape can be obtained,³⁵ as evidenced in the TEM images shown in Figure 3 and in the examples compiled in Table 1. On the other hand, NH₄OH also plays an important role for controlling the size of these NPs, as evidenced in previous works by Iraqui et al.³⁶ and Cai et al.³⁷ These authors prepared NiFe₂O₄ NPs with average sizes of 11.3 and 8 nm, respectively, through a solvothermal method assisted by NH₄OH in the absence of an SDA. The NiFe₂O₄ NPs grown over GO by Cai et al.³⁷ had average size similar to that we obtained for our NiFe₂O₄ and NiFe₂O₄/GO samples. The mechanism of size control in the NH₄OH-assisted synthesis process is probably through the formation of intermediate species (several), as explained in Section 3.1. The average size of the NiFe₂O₄ NPs grown over GO in the present work is smaller than the average size of NiFe₂O₄ NPs grown over GO in the majority of the previously reported works. For example, Sawai et al.³⁸ and Liang et al.³⁹ obtained NiFe₂O₄ NPs over rGO with mean sizes of 23 and 11 nm, respectively, using a hydrothermal method. Ren et al.⁴⁰ synthesized CoFe₂O₄ NPs with a 35 nm average size by a hydrothermal method in the presence of PVP and urea followed by Ar annealing at 550 °C. Yin et al.⁴¹ obtained CoFe₂O₄ NPs of 11 nm mean size grown over rGO by a solvothermal process in the presence of N₂H₄. Only a few works reported the synthesis of NiFe₂O₄/GO or NiFe₂O₄/rGO nanocomposites with an average size smaller than 10 nm.^{42,43} Some additional works dealing with the synthesis of metal ferrites are listed in Table 1.

3.5. Raman and FTIR Spectroscopy Analysis. First-principle calculations of spinel structures such as NiFe₂O₄ indicate that they have five active modes in the Raman spectrum.⁵⁰ Room temperature Raman spectrum of the NiFe₂O₄ nanoparticles prepared in this work are presented in Figure 4a. The NiFe₂O₄ NPs exhibited five Raman bands located around 203, 320, 474, 541, and 684 cm⁻¹. In addition, a low-intensity and broad dispersion band appeared around 1239 cm⁻¹, which corresponds to an overtone of the band located at 684 cm⁻¹. Whereas the Raman bands appearing around 203, 474, and 541 cm⁻¹ have T_{2g} symmetry, the Raman band appearing at 320 cm⁻¹ has T_{2g} symmetry. The totally symmetric mode (A_{1g}) is located around 684 cm⁻¹.

The Raman spectra of the NiFe₂O₄ nanoparticles grown over graphene oxide along with the Raman spectra of bare GO are presented in Figure 4b. To highlight the differences among the Raman spectra of NiFe₂O₄ and its nanocomposite with GO, the amplified Raman spectra of the two samples are presented in Figure S5 (Supporting Information). Whereas the Raman shift of the T_{2g}(2) band appeared at 474 cm⁻¹ for the bare NiFe₂O₄ NPs, it is located around 479 cm⁻¹ for the

nanocomposite (Figure 4b). Similarly, the band associated with the A_g mode in NiFe₂O₄ shifted from 684 to 700 cm⁻¹ in the nanocomposite. Chandramohan et al. reported that the position of the A_g mode in CoFe₂O₄ nanoparticles shifts progressively from 677 to 695 cm⁻¹ with the progressive reduction of exciting laser power.⁵¹ Therefore, the shift of this Raman band toward a higher wavenumber for NiFe₂O₄ in the presence of GO is probably due to the rapid dissipation of the heat generated by laser illumination over the NPs toward GO support. This fast heat dissipation avoids the increase in temperature of the sample, shifting the Raman band toward a higher wavenumber. The other possibility for the blue-shift of the A_g peak is due to the smaller size of the NPs grown over GO, as has been discussed in Section 3.2.

Graphene oxide in the nanocomposite is recognized by the presence of the D (defective) and G (graphitic) bands in its Raman spectrum. The position of the D band depends on the wavelength of the used laser source.⁵² In the present work, the D and G bands in the used GO appeared around 1334 and 1594 cm⁻¹ (Figure 4b), respectively, which are in accordance with their positions in GO reported previously for the excitation with 633 nm laser beam.⁵³ Once the graphene oxide was partially reduced through the hydrothermal treatment to generate reduced GO, the G band was displaced from 1594 to ca. 1600 cm⁻¹ (Figure S5b, Supporting Information), as has been reported earlier.⁵⁴ Ferrari et al.⁵⁴ and Dresselhaus et al.⁵⁵ reported the appearance of a new Raman dispersion band around 1620 cm⁻¹ (called D' band) in disordered graphitic materials (e.g., graphene oxide), arising as a result of double resonance. The double resonance is an electronic transition occurring as an intravalley scattering at point K (or K') in the phonon dispersion branch in defective graphene.⁵⁴ This D' band was detected in our NiFe₂O₄/GO nanocomposite as a right shoulder to the G band (Figure S5b, Supporting Information). On the other hand, the intensity ratio of the D and G band (I_D/I_G) is a useful parameter to know the degree of oxidation/reduction of the graphene oxide. The I_D/I_G ratios for the graphene oxide and NiFe₂O₄/GO were estimated to be about 1.31 and 1.22, respectively, which indicate a partial reduction of GO in the NiFe₂O₄/GO nanocomposite.

FTIR spectra of the GO, NiFe₂O₄, and NiFe₂O₄/GO samples are presented in Figure 4c, and corresponding vibrational bands are assigned as presented in Table 2. The bands associated with GO that appeared in its FTIR spectrum are very similar to those reported by Jiao et al.⁵⁶ In the spectrum for the NiFe₂O₄ nanoparticles, the band that appeared around 626 cm⁻¹ corresponds to the stretching vibration of Fe–O bonds. The bands appearing between 3400 and 1630 cm⁻¹ are associated with the stretching and bending of the O–H groups present in the adsorbed water. Bands located around 1710 and 1362 cm⁻¹ are attributed to the C=O and C–O stretching, respectively, which probably appeared because of the presence of acetate (CH₃COO⁻) ions bonded to the surface of NiFe₂O₄ nanoparticles. These ions came from sodium acetate used as reagent. On the other hand, in the FTIR spectrum of the NiFe₂O₄/GO sample, along with the appearance of the characteristic Fe–O bond at 626 cm⁻¹, there appeared several absorptions bands corresponding to GO. Interestingly, the band detected at 1713 cm⁻¹ in the GO was not observed in the NiFe₂O₄/GO nanocomposite, indicating that the carbonyl group (C=O) in GO was reduced during the synthesis of the nanocomposite. The bands located at 1580

Table 2. Band Positions (cm⁻¹) and Their Corresponding Assigned Vibrations for the GO, NiFe₂O₄, and NiFe₂O₄/GO Samples⁵⁷

GO	NiFe ₂ O ₄	NiFe ₂ O ₄ /GO	band assignment
3429	3400		$\nu(\text{O-H})$ from alcohol groups or water
2932, 2862	2918	2908	$\nu(\text{CH}_2)$
1713, 1686	1710		$\nu(\text{C=O})$ from a carboxylate group
		1652	$\nu(\text{C=C})$ from the aromatic rings in GO
1630	1630		$\delta(\text{O-H})$ from water or $\nu(\text{C=C})$ from the aromatic rings in GO
		1580	$\nu(\text{C=N})$ from the N-doped aromatic rings in GO
1420			
1362	1362	1368	$\nu(\text{C-O})$ from carboxylate or alcohol groups
		1285, 1272	$\nu(\text{C-N})$ from the N-doped aromatic rings in GO
1224	1224	1219	$\nu(\text{C-O})$ from a carboxylate group or aryl alcohol
1041	1048	1030	$\nu(\text{C-C})$ from a carboxylate group or GO
		1023	$\nu(\text{C-C})$ from GO
858	848		$\delta(\text{C-H})$ from the aromatic rings in GO
	626	626	Fe-O from nickel ferrite

and 1285 cm⁻¹ are attributed to the C=N and C-N stretching vibrations,⁵⁷ which suggest the presence of N-doped aromatic rings at the surface of GO in the nanocomposite.

3.6. X-ray Photoelectron Spectroscopy (XPS) Analysis. The survey spectra of NiFe₂O₄ and NiFe₂O₄/GO samples revealed the presence of Ni, Fe, O, and C elements, as expected. In addition, the peak attributed to the N 1s orbital (BE 399.5 eV) was detected in the NiFe₂O₄/GO nanocomposite, which is associated with the functionalization of graphene oxide with amine or amide groups (Figure 5a).⁵⁸ Ederer et al.²⁵ reported that the N 1s emission from amine (C-NH₂) and amide (HN-C(=O)) groups appear at 399.5 ± 0.3 and 399.9 ± 0.1 eV, respectively. The high-resolution spectrum of the N 1s emission for the NiFe₂O₄/GO nanocomposite is presented in Figure 6S (Supporting Information). The deconvolution of the XPS peak generated two components centered at 398.5 and 399.5 eV. Whereas the component centered at 398.5 eV is attributed to pyridinic nitrogen, the component centered at 399.5 eV is attributed to aminic (C-NH₂), amide, or pyrrolic nitrogen.^{59,60} The absence of a peak around 199 eV in the survey spectrum is associated with the Cl 2p orbital discarded in the presence of NH₄Cl impurity in the sample. Therefore, the appearance of N 1s emission peak at 399.5 eV in the survey spectrum indicates that the graphene oxide in the NiFe₂O₄/GO nanocomposite has been functionalized with amine or amide groups during the hydrothermal treatment.²⁵ The high relative intensity of the nitrogen peak in the survey spectrum suggests that in the NiFe₂O₄/GO nanocomposite, the reduced graphene oxide is doped with nitrogen atoms or functionalized with amine (-NH₂) or amide (-CONH₂) groups. The functionalization of graphene oxide during hydrothermal treatment was achieved by NH₃ present at moderate pressure, which could react with the electron-deficient carbon atoms in the carbonyl (C=O), aldehyde (H-C=O), or alcohol (C-OH) groups present in the graphene oxide.

On the other hand, a small shift of the Ni 2p_{3/2} and Ni 2p_{1/2} peaks toward higher BE could be observed for the nanocomposite sample compared with their positions in the pure NiFe₂O₄ sample (Figure 5b). Such a difference in BE positions of the Ni 2p_{3/2} and Ni 2p_{1/2} peaks is probably due to the presence of a considerable amount of OH groups at the surface of small (~6 nm) NiFe₂O₄ NPs formed over GO. In fact, the BEs of the Ni 2p_{3/2} and Ni 2p_{1/2} peaks for transition metals have been seen to be slightly higher for metal hydroxides than for the corresponding metal oxides.⁵⁸ On the other hand, the BE positions of the Fe 2p_{3/2} and Fe 2p_{1/2} peaks for the composite correspond well to Fe³⁺ ions, as expected in metal ferrites (Figure 5c). The emission bands corresponding to the C 1s orbital for the NiFe₂O₄ and NiFe₂O₄/GO samples are similar in shape and position, indicating that C=O (ketone), H-C=O (aldehyde), and O-C=O carboxylate groups in the samples remain in low concentrations (Figure 5d), as expected in reduced GO.¹⁸ However, the XPS results confirm that graphene oxide was partially reduced. The deconvoluted C 1s bands for the two samples are presented in Figure 5e,f. Deconvolution of the C 1s peak in NiFe₂O₄ generated four component peaks associated with the presence of -C-C- (or -C=C-), C-OH, C=O, and O=C=O bonds of adventitious carbon (Figure 5e). The BE, relative area, and fwhm values of the -C-C- (or -C=C-), C-OH, C=O, and O=C=O bonds estimated for the NiFe₂O₄ sample are presented in Table S2 (Supporting Information). On the other hand, a deconvolution of the C 1s peak that appeared for the NiFe₂O₄/GO nanocomposite generates six component bands. The functional group associated with each peak is shown in Figure 5f. The fwhm values of the dispersion bands are presented in Table S2 (Supporting Information). Notably, the component peak centered at 285.63 eV indicates the presence of C-O-C and C-N bonds of the ether and amine functional groups. The presence of ether functional group in the reduced GO makes sense, as it is well-known that this group is very difficult to be reduced at low temperatures and atmospheric pressures in the absence of a proper catalyst.⁶¹

Finally, a comparison of the O 1s peaks revealed for the NiFe₂O₄ and NiFe₂O₄/GO samples clearly evidence the presence of OH groups at the surface of NiFe₂O₄ NPs (Figure 5g). It should be mentioned that the O 1s emission from OH groups present in GO of the nanocomposite also appears around 530.6 eV. Deconvolution of the O 1s peak for both samples and corresponding relative areas of the component bands are presented in Figures 5h,i and Table S2 (Supporting Information), respectively. The obtained XPS results confirmed that the presence of M-OH groups is higher in the NiFe₂O₄/GO nanocomposite than in the bare NiFe₂O₄ NPs.

3.7. Magnetic Characterization. The magnetic moment versus applied magnetic field (*M-H*) curves for NiFe₂O₄ and NiFe₂O₄/GO samples recorded at different temperatures are presented in Figure 6a,b. Corresponding values of saturation magnetization (*M_s*) and coercive field for the samples are presented in Figure 6c. The NiFe₂O₄ NPs exhibited *M_s* values of 62.2 and 52.4 emu/g at 10 and 300 K, respectively, indicating about 15.7% reduction of *M_s* value due to the increase of temperature from 10 to 300 K. Likewise, the NiFe₂O₄/GO composite exhibited *M_s* values of 47.8 and 31.7 emu/g at 10 and 300 K, respectively, which correspond to a decrease of about 33.6% in the *M_s* values due to the increase of temperature. The considerable difference in the two percentages (15.7 and 33.6%) is probably due to the smaller size of

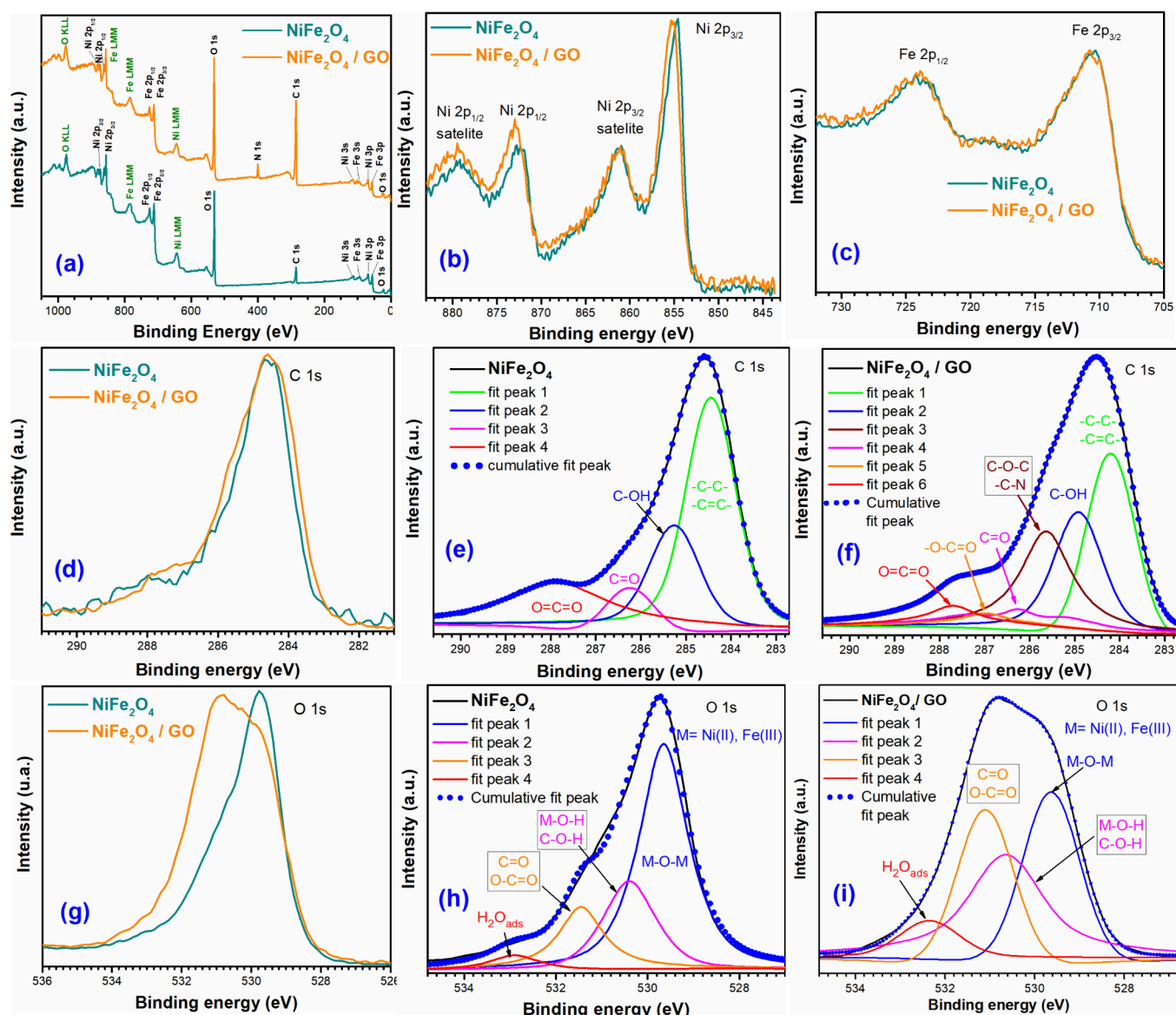


Figure 5. XPS spectra of the NiFe_2O_4 and $\text{NiFe}_2\text{O}_4/\text{GO}$ samples. XPS survey spectra of NiFe_2O_4 NPs, and $\text{NiFe}_2\text{O}_4/\text{GO}$ nanocomposite (a) and normalized high-resolution spectra of selected XPS peaks for both samples (b–d, g). (e, f, h, i) Deconvoluted C 1s and O 1s emission bands of the NiFe_2O_4 and $\text{NiFe}_2\text{O}_4/\text{GO}$ samples. The areas of the component (fitted) bands are presented in Table S2 of SI.

the NiFe_2O_4 NPs grown over GO (6.2 ± 1.0 nm) than that of the bare-grown NiFe_2O_4 NPs (13.8 ± 2.9 nm). In the smaller NiFe_2O_4 NPs, the spin alignment is easier to be destroyed by thermal energy during heating, which progressively decreases the M_s value. Both the bare-grown and GO-supported NiFe_2O_4 NPs exhibited a superparamagnetic behavior.

On the other hand, at 10 K, the M_s of the $\text{NiFe}_2\text{O}_4/\text{GO}$ nanocomposite is 23.1% lower than that of the bare NiFe_2O_4 sample. This difference is mainly due to the presence of GO (30% nominal) in the nanocomposite, which does not contribute significantly to the M_s value. In fact, the contribution of GO to the M_s value of the sample at 10 K is smaller than 0.8 emu/g (Figure S7 and Supporting Information).

The irreversibility temperature (T_{irr}), i.e., the point at which the zero-field-cooling (ZFC) and field-cooling (FC) magnetization curves split, for the NiFe_2O_4 sample is above 300 K (Figure 6d). However, the T_{irr} for the $\text{NiFe}_2\text{O}_4/\text{GO}$ nanocomposite is around 60 K. Such a lower T_{irr} value for the

$\text{NiFe}_2\text{O}_4/\text{GO}$ nanocomposite is probably due to the combined effect of the low coercive field (162 Oe at 10 K) and the small size of the NiFe_2O_4 NPs dispersed over GO.

3.8. N_2 Adsorption–Desorption Analysis. The adsorption–desorption isotherms of the metal ferrite nanoparticles and nanocomposites measured at 77 K are presented in Figure S8 (Supporting Information). The N_2 physisorption curves exhibited type IV isotherms, which are associated with capillary condensation of N_2 at mesopores.⁶² The bare NiFe_2O_4 NPs exhibited type III hysteresis loops, corresponding to materials with slit-shaped pores. Graphene oxide and the $\text{NiFe}_2\text{O}_4/\text{GO}$ nanocomposite exhibited type IV hysteresis loops, which are associated with narrow slit-shaped pores.⁶² These narrow slit-shaped pores are present between the layers of pristine graphene oxide, between the layers of graphene oxide (GO) in the nanocomposite, and between the NPs grown over GO. A steep region in the desorption branch leading to the lower closure point of the hysteresis loop for $\text{NiFe}_2\text{O}_4/\text{GO}$ nanocomposite can be observed around $p/p_0 \approx 0.42$ (Figure

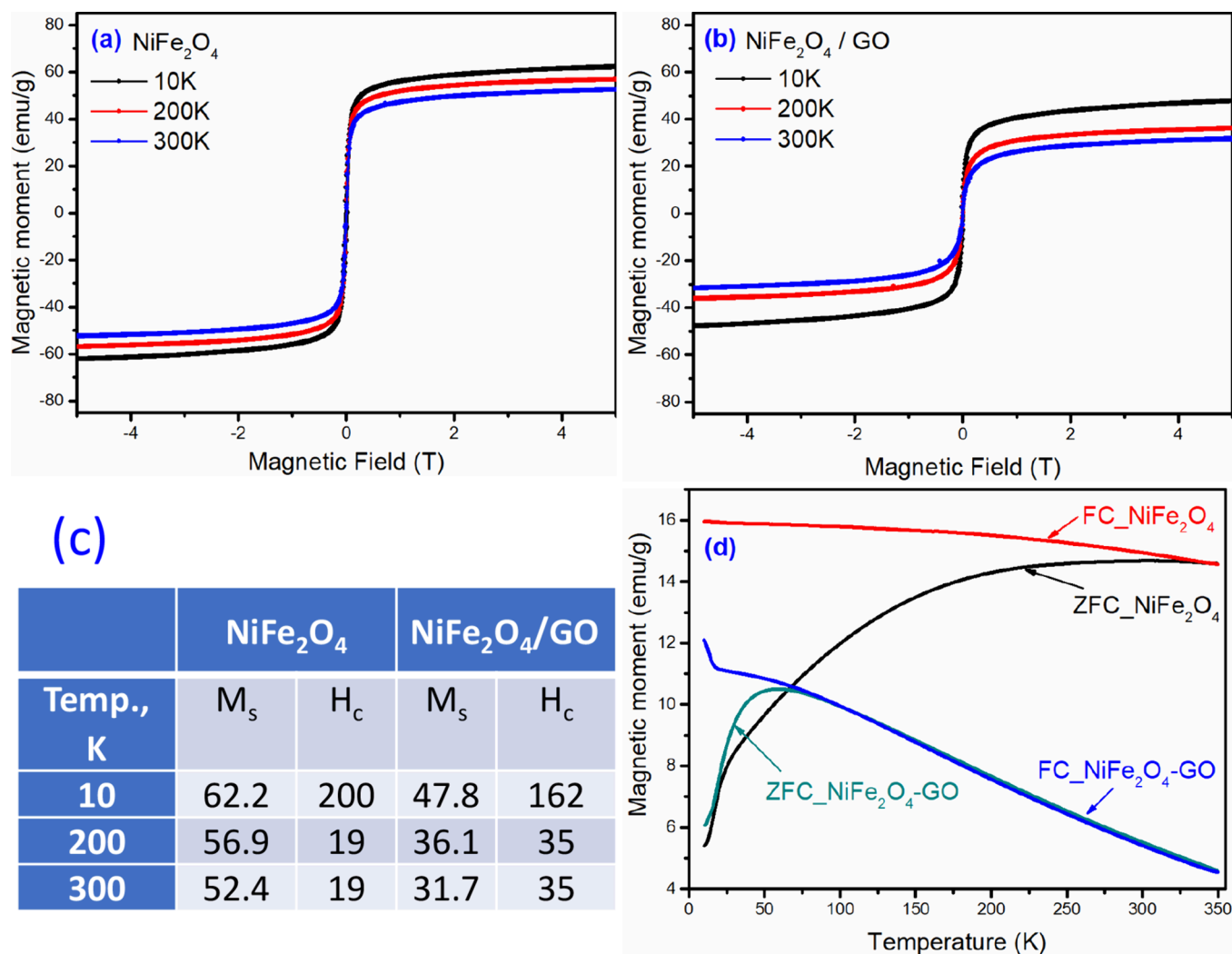


Figure 6. Magnetization vs applied magnetic field ($M-H$) curves for the (a) NiFe_2O_4 NPs and (b) $\text{NiFe}_2\text{O}_4/\text{GO}$ nanocomposite. (c) Saturation magnetization (M_s , emu/g) and coercive fields (H_c , Oe) values for the NiFe_2O_4 nanoparticles and $\text{NiFe}_2\text{O}_4/\text{GO}$ nanocomposite at different temperatures. (d) Zero-field-cooling (ZFC) and field-cooling (FC) magnetization curves for the NiFe_2O_4 nanoparticles and $\text{NiFe}_2\text{O}_4/\text{GO}$ nanocomposite.

S8b, Supporting Information), as frequently happens when N_2 is used for the measurements.⁶² However, this steep region in the desorption branch for pure NiFe_2O_4 sample occurred at approximately $p/p_0 \approx 0.63$ (Figure S8a, Supporting Information). The difference in the p/p_0 value at which the steep region appeared might be due to the narrower pore size distribution in the nanocomposite than in the samples of pure metal ferrite (Figure S8d, Supporting Information).

The BET estimated surface areas for NiFe_2O_4 ($84.08 \text{ m}^2 \text{ g}^{-1}$), $\text{NiFe}_2\text{O}_4/\text{GO}$ ($90.05 \text{ m}^2 \text{ g}^{-1}$), and graphene oxide ($3.27 \text{ m}^2 \text{ g}^{-1}$) revealed a bit larger specific surface area of the nanocomposite sample than the bare NiFe_2O_4 NPs sample (Figure S8a–c, Supporting Information). The difference in surface area is probably due to the smaller size and better dispersion of nickel ferrite NPs grown over GO. The lower magnetic moment of the composite might have also contributed to the cause. As can be seen in Figure 6c, the magnetic moment of the bare nickel ferrite nanoparticles is 39% lower than that of the ones grown over GO.

3.9. Cr(III) Ion Adsorption by Nickel Ferrite NPs and Nickel Ferrite/GO Nanocomposite. Figures 7a–c shows the UV–vis absorption spectra of aqueous Cr(III) ion

solutions (after oxidizing to CrO_4^{2-} by H_2O_2) collected at different time intervals of adding the adsorbents. The absorption spectra corresponding to the NiFe_2O_4 and $\text{NiFe}_2\text{O}_4/\text{GO}$ samples revealed a band corresponding to the CrO_4^{2-} ions at 373 nm (Figures 7a,b). The band appearing below 300 nm corresponds to the H_2O_2 species. As can be observed, for the aqueous Cr(III) ion solutions exposed to NiFe_2O_4 and $\text{NiFe}_2\text{O}_4/\text{GO}$ adsorbents, the intensity of the absorption band corresponding to CrO_4^{2-} ion progressively decreased with exposure time (Figures 7a,b). The lower the intensity of the band associated with the CrO_4^{2-} ions located at 373 nm is, the better is the performance of the adsorbent for the removal of Cr(III) ions from water.

For comparison, the as-prepared graphene oxide was also used as an adsorbent of Cr(III) ions. It can be seen that the absorbance of CrO_4^{2-} ions diminished considerably in the first 10 min of exposure of the solution to the graphene oxide (Figure 7c). However, the absorbance remained almost unchanged for a longer exposure time. This behavior suggests that an ion exchange occurred between the H^+ ions adsorbed in the graphene oxide and the Cr(III) ions present in the aqueous solution. As has been mentioned in the Experimental

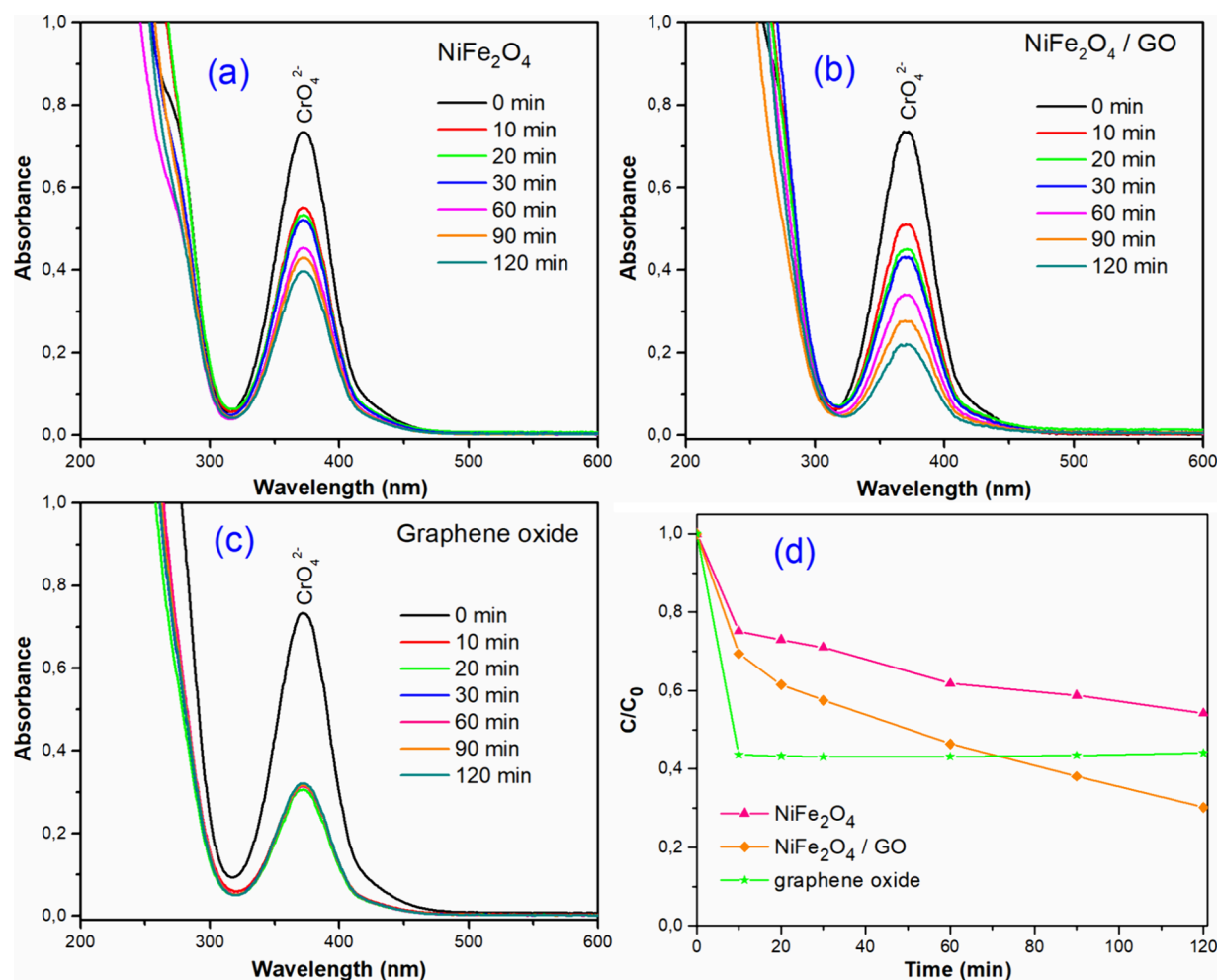


Figure 7. (a–c) UV–vis absorption spectra of aqueous Cr(III) ion solutions (after oxidizing to CrO_4^{2-} by H_2O_2) collected at different time intervals of adding the adsorbents (a) NiFe_2O_4 , (b) $\text{NiFe}_2\text{O}_4/\text{GO}$, and (c) GO. The initial concentration of Cr(III) ions in the solution was 10 ppm. Fifty milligrams of the adsorbent was added in 100 mL of Cr(III) ion solution. C stands for the concentration of Cr(III) ions in the solution at a given time, and C_0 is its initial concentration (10 ppm). Fifty milligrams of each adsorbent (NiFe_2O_4 , $\text{NiFe}_2\text{O}_4/\text{GO}$, GO) was used.

Section, during preparation, the graphene oxide was washed through centrifugation until the pH of the supernatant reaches ~ 3.5 . Such a low pH favors the adherence of H^+ ions at the surface of graphene oxide.

To determine the concentration of Cr(III) in water, a calibration curve was prepared by utilizing Cr(III) solutions of different concentrations (from 0.5 to 20 ppm) (Figure S9, Supporting Information). The variations of the ratio of Cr(III) ion concentration in solution (C) with respect to its initial concentration (C_0) with the time of exposure of the adsorbents (NiFe_2O_4 NPs and $\text{NiFe}_2\text{O}_4/\text{GO}$ nanocomposites) are presented in Figure 7d. After 120 min of exposure, the lowest C/C_0 ratio was obtained for the $\text{NiFe}_2\text{O}_4/\text{GO}$ nanocomposite, indicating that this nanocomposite exhibits the best performance among the studied nanostructures for the removal of Cr(III) ions from water.

The capacity of nanomaterials to adsorb metal ions from aqueous solutions depends on the charge present on their surface.⁶³ One parameter used to represent this charge is the zeta potential, which indicates the sign and magnitude of the surface charge of nanomaterials suspended in a liquid. In this study, the zeta potential values obtained for the NiFe_2O_4 nanoparticles and $\text{NiFe}_2\text{O}_4/\text{GO}$ nanocomposite suspended in

deionized water at pH 6.5 were $+26 \pm 3.8$ and -18.0 ± 4.8 mV, respectively. The nanocomposite's slightly negative charge at pH 6.5 suggests that Cr(III) ions, which have a positive charge, are expected to be adsorbed more efficiently on the $\text{NiFe}_2\text{O}_4/\text{GO}$ than on the bare NiFe_2O_4 nanoparticles due to electrostatic attraction. It is worth noting that a positive zeta potential value ($\sim +26$ mV) at pH 6.5 was also reported for NiFe_2O_4 nanoparticles by Bhosale et al.,⁶⁴ whereas Sukumar et al.⁶⁵ reported a negative zeta potential value (~ -6 mV) for NiFe_2O_4 nanostructures.

To study the effect of the adsorbent loading, we performed the adsorption of Cr(III) ions using several $\text{NiFe}_2\text{O}_4/\text{GO}$ loadings (Figure 8a–e). As can be seen in Figure 8, the removal of the Cr(III) ions increased progressively with the increase in adsorbent loading. For the 150 mg loading of $\text{NiFe}_2\text{O}_4/\text{GO}$ nanocomposite, the vast majority ($>96\%$) of the chromium ions were removed from the solution in 90 min (Figure 8f). The concentration of Cr(III) ions after removal of the nanocomposite was close to 0.1 mg L^{-1} , which is close to the allowed level of Cr(III) ions in drinking water (0.1 ppm). A higher loading of the adsorbent can easily reduce the Cr(III) ions in water below the 0.1 mg L^{-1} limit. However, it must be noted that the residual Cr(III) ion concentration in the

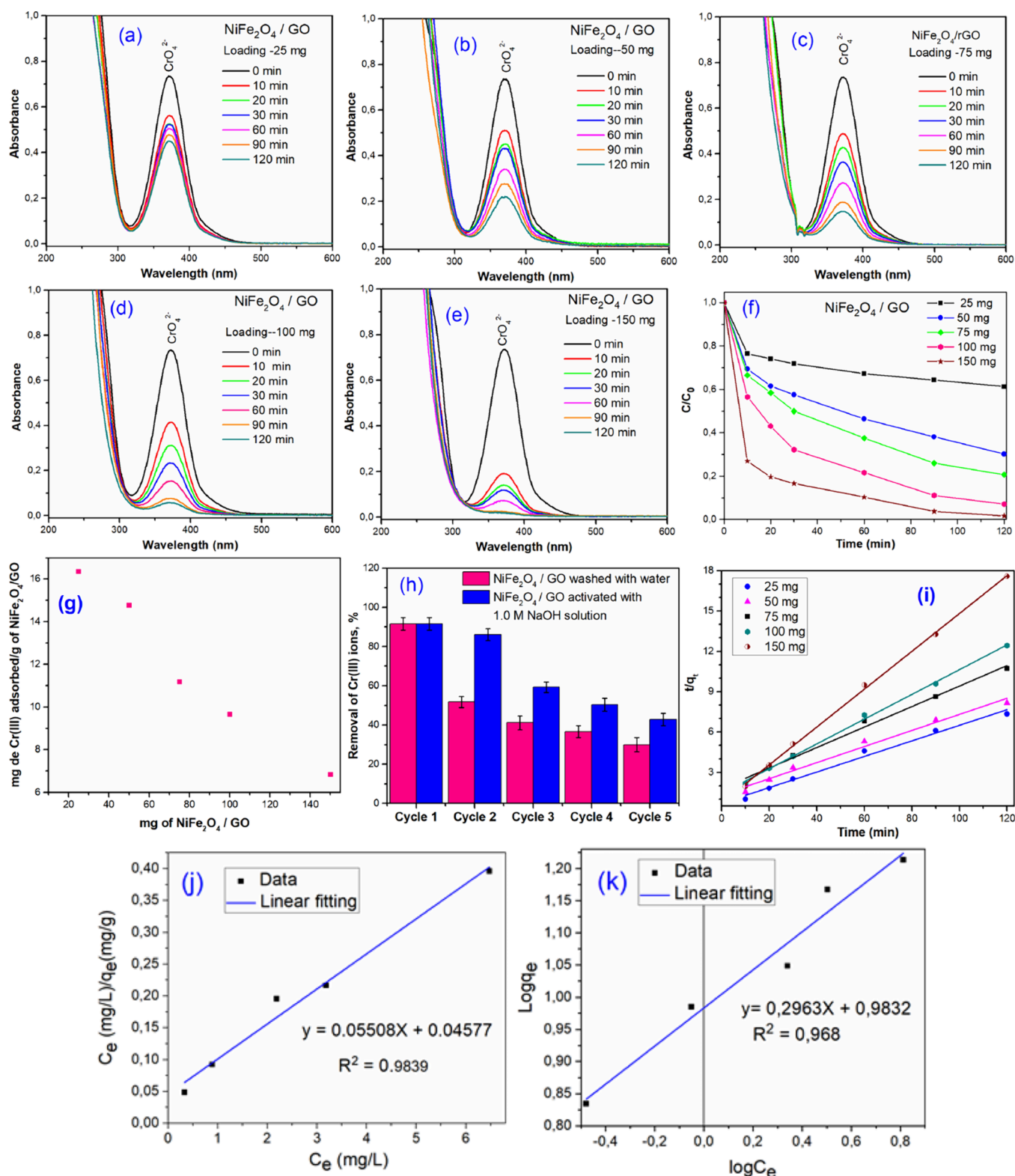


Figure 8. (a–e) UV–vis absorption spectra of aqueous Cr(III) ion solutions (after oxidizing to CrO_4^{2-} by H_2O_2) collected at different time intervals of adding the adsorbent $\text{NiFe}_2\text{O}_4/\text{GO}$ at (a) 25 mg, (b) 50 mg, (c) 75 mg, (d) 100 mg, and (e) 150 mg loading in 100 mL of solution. (f) Variation of C/C_0 with adsorbent exposure time. (g) Amount of Cr(III) ion removed per gram of adsorbent for different loadings after 120 min of exposure. (h) Reusability tests of the $\text{NiFe}_2\text{O}_4/\text{GO}$ nanocomposite using an adsorbent loading of 100 mg (in 100 mL of chromium ion solution) and 120 min exposure time. (i) t/q_t versus time graphs associated with the pseudo-second-order adsorption of Cr(III) ions on the $\text{NiFe}_2\text{O}_4/\text{GO}$ composite at different loadings. q_t represents the adsorption capacity at a given time (t). (j) Langmuir and (k) Freundlich isotherms for the adsorption of Cr(III) ions over the surface of the $\text{NiFe}_2\text{O}_4/\text{GO}$ nanocomposite.

aqueous solution after removing the adsorbent (NiFe₂O₄/GO) in the present case was much lower than the values reported for ferrihydrite (~1 mg L⁻¹ for adsorbent dosage of 1.4 g L⁻¹)⁶ and Co/Fe layered double hydroxide (<1.5 mg L⁻¹ for adsorbent dosage of 9 g L⁻¹).⁶⁶

The Cr(III) ion adsorption capacity of the NiFe₂O₄/GO composite was evaluated quantitatively by estimating the amount of Cr(III) ions removed from the solution per gram of the adsorbent after 120 min of its exposure. As can be seen in Figure 8g, the adsorption capacity of the nanocomposite diminishes with the increase in its loading in solution. The maximum Cr(III) ion adsorption capacity (17 mg g⁻¹) of the NiFe₂O₄/GO composite was obtained for its 25 mg loading. The NiFe₂O₄/GO composite prepared in the present study exhibited better Cr(III) ion adsorption performance from its aqueous solution than several natural adsorbent materials such as vineyard pruning waste (12.45 mg g⁻¹), *Pinus sylvestris* bark (8.69 mg g⁻¹), rice husk (0.77 mg g⁻¹), palm flower (6.24 mg g⁻¹), and saw dust (5.52 mg g⁻¹) reported in the literature.⁶⁸ However, the Cr(III) ion adsorption capacity of our NiFe₂O₄/GO composite (Figure 8g) is within the range reported for some inorganic adsorbents such as sodium titanate nanotubes,²¹ mesoporous SBA-15 functionalized with 2-acetylthiophene,¹³ Co/Fe layered double hydroxide,⁶⁶ humic acid modified Ca-montmorillonite,¹² graphene oxide,¹⁵ and graphene oxide/alginate hydrogel membrane.⁴ Moreover, the nanocomposite could be easily removed from Cr(III) ion solutions by using a commercial magnet.

The reusability tests were carried out for the NiFe₂O₄/GO nanocomposite sample after simple washing and after its chemical activation at the end of each adsorption test. As can be seen in Figure 8h, the Cr(III) ion capture efficiency of the used adsorbent is much higher when it is activated by a NaOH solution after each adsorption cycle. When the NiFe₂O₄/GO nanocomposite was washed only with deionized water, its Cr(III) ion removal capacity decreased from 91 to 30% after five cycles (Figure 8h). However, when the nanocomposite was activated with 1.0 NaOH solution, its Cr(III) ion removal capacity decreased from 91 to 43% after five cycles. Sodium hydroxide (NaOH) reacts with the Cr(III) species that are attached to the surface of the used samples, forming Cr(OH)₄⁻ species. These species then dissolve in the washing water, effectively removing the adsorbed Cr(III) ions from the adsorbent surface.

The obtained result is very similar to the observation of Krishna Kumar et al.²² who utilized MoS₂@Fe₃O₄ nanoparticles for the removal of Cr(VI) ions from water, finding NaOH activation as an efficient process for the reutilization of the adsorbent. It should be noted that the adsorption capacity of the GO/alginate hydrogel membrane utilized for Cr(III) ion capture from aqueous solution was seen to diminish by 50% after four reusability tests.⁴

To study the rate of Cr(III) ion adsorption over the NiFe₂O₄/GO nanocomposite, Lagergren's pseudo-first-order model for liquid–solid systems was utilized.⁶⁹ In this model, the adsorbate capture rate of an adsorbent is expressed by

$$\frac{dq_t}{dt} = k_1(q_e - q_t) \quad (1)$$

where k_1 is the rate constant of the pseudo-first-order adsorption and q_e and q_t are the amount of Cr(III) ions adsorbed on the adsorbent at equilibrium and at a given time t

(mg g⁻¹). By integration of eq 1 considering the boundary conditions ($q_t = 0$ at $t = 0$), we can obtain the equation

$$\log(q_e - q_t) = \log q_e - \frac{k_1}{2.303}t \quad (2)$$

Lagergren's pseudo-first-order plot for the adsorption of Cr(III) ions is shown in Figure S10 (Supporting Information). The estimated q_e and k_1 values for the NiFe₂O₄/GO nanocomposite are presented in Table S3 (Supporting Information). However, the correlation coefficient (R^2) obtained for the fitting curves is not very close to the ideal value (1.0), which indicates that the Cr(III) ion adsorption kinetics at the surface of the composite does not obey the pseudo-first-order model of Lagergren. On the other hand, Ho and McKay proposed a pseudo-second-order kinetic model for the adsorption of substances on the surface of the solids,⁶⁷ which follows eq 3. After the integration of this equation and a rearrangement, we obtain eq 4:

$$\frac{dq_t}{dt} = k_2(q_e - q_t)^2 \quad (3)$$

$$\frac{t}{q_t} = \frac{1}{k_2(q_e)^2} + \frac{1}{q_e}t \quad (4)$$

where t is the adsorption time, k_2 is an adsorption constant, q_t is the adsorption (mg g⁻¹) at a given time, and q_e is the adsorption capacity at equilibrium for the adsorbent. The plot of t/q_t for the NiFe₂O₄/GO nanocomposite is shown in Figure 8i. As can be seen, the data points produced good linear fits for all the values of adsorbent loading. In fact, the correlation coefficient (R^2) obtained for these fits is larger than 0.985, which suggests that the adsorption mechanism of Cr(III) ions over the nanocomposite follows a pseudo-second order. The estimated adsorption constant (k_2) and adsorption capacity at equilibrium (q_e) of the process are presented in Table S3 (Supporting Information). The largest q_e value (17 mg of Cr(III)/g of adsorbent) was obtained for the loading of 25 mg of the NiFe₂O₄/GO nanocomposite.

3.10. Langmuir and Freundlich Adsorption Isotherms. To understand the mechanism of Cr(III) ion adsorption on NiFe₂O₄/GO, we tested the Langmuir adsorption model, considering eq 5:

$$\frac{C_e}{q_e} = \frac{1}{K_L q_m} + \frac{C_e}{q_m} \quad (5)$$

where C_e is the adsorbate equilibrium concentration, q_e is the amount of Cr(III) ions adsorbed on the adsorbent at equilibrium, q_m is the maximum adsorption capacity, and K_L is the adsorption constant related to the binding strength.⁷⁰ Using eq 5 and the slope ($1/q_m$) of the Langmuir adsorption isotherm shown in Figure 8j, the adsorption capacity of the adsorbent was obtained ($q_m = 18.1$ mg of Cr(III)/g of adsorbent). The high R^2 value (0.9839) obtained by fitting of the data indicates that the adsorption of Cr(III) is in accordance with the Langmuir model. Likewise, the K_L value estimated from the intercept was 1.20 L/mg, which is larger than those reported for mesoporous SBA-15 functionalized with 2-acetylthiophene (0.2467 L/mg)¹³ and MoS₂@Fe₃O₄ nanocomposite (0.13 L/mg)²² but smaller than those reported for the adsorbent ferrihydrite (1.65 L/mg)⁶ and sodium titanate nanotubes (3.61 L/mg).²¹ The Freundlich isotherm model is also frequently used for the adsorption of ions and

was developed for adsorption over heterogeneous surfaces. This model is based on eq 6:

$$\log q_e = \log K_F + \frac{1}{n} \log C_e \quad (6)$$

where q_e and C_e were as defined previously, K_F is a distribution coefficient, and n is the Freundlich equilibrium coefficient representing the adsorption intensity.²¹ By plotting $\log(q_e)$ versus $\log(C_e)$ and making a linear fitting (Figure 8k), the K_F (9.62) and n (3.37) values were obtained. The obtained R^2 value (0.968) for the fitting using the Freundlich isotherm was lower than that obtained for the Langmuir isotherm. Accordingly, the adsorption of Cr(III) ions over the NiFe₂O₄/GO composite is better adjusted to the Langmuir model (which was developed for homogeneous surfaces) than to the Freundlich model (which was developed for heterogeneous surfaces).

4. CONCLUSIONS

We demonstrate the fabrication of small (~7 nm average size) and well-dispersed NiFe₂O₄ nanoparticles over exfoliated graphene oxide sheets by a low-temperature hydrothermal process utilizing ammonium hydroxide, PVP, and sodium acetate as pH-, shape-, and size-controlling agents. The NiFe₂O₄/GO nanocomposite revealed its superparamagnetic behavior, with almost zero (~35 Oe) coercive field at room temperature, although its saturation magnetization (M_s) is slightly lower than that of bare NiFe₂O₄ nanoparticles due to the GO support. The superparamagnetic nanocomposite was used as an efficient magnetically separable adsorbent for removing Cr(III) ions dissolved in water. The nanocomposite could remove >91% of chromium ions from its aqueous solution, with a moderate adsorption capacity of 17.0 mg/g. Utilizing the magnetically separable nanocomposite, the Cr(III) ion level in water could be reduced to the level close to the EPA-prescribed limit (0.1 mg L⁻¹). Finally, we demonstrate a simple optical method for detecting Cr(III) ions in water, which is much easier to use and less expensive in comparison to the conventional methods such as atomic absorption spectroscopy and inductively coupled plasma spectroscopy.

■ ASSOCIATED CONTENT

SI Supporting Information

The Supporting Information is available free of charge at <https://pubs.acs.org/doi/10.1021/acsanm.3c03618>.

XRD pattern of NiFe₂O₄ NPs and NiFe₂O₄/GO nanocomposite before washing them with methanol or water; EDS and amplified Raman spectra for the NiFe₂O₄ NPs and the NiFe₂O₄/GO nanocomposite; a table with binding energies, fwhm, and area (%) of the components of the representative XPS emissions for the NiFe₂O₄ and NiFe₂O₄/GO samples; N₂ adsorption-desorption isotherms; magnetization curves for the GO; UV-vis absorption spectra of Cr(III) ion solutions recorded after oxidizing to CrO₄²⁻ ions by H₂O₂; and Lagergren's plots for Cr(III) ion adsorption by NiFe₂O₄/GO (PDF)

■ AUTHOR INFORMATION

Corresponding Author

Umapada Pal – Instituto de Física, Benemérita Universidad Autónoma de Puebla, Puebla, Pue 72570, Mexico; orcid.org/0000-0002-5665-106X; Email: upal@ifuap.buap.mx

Authors

Jose Luis Ortiz-Quiñonez – Instituto de Física, Benemérita Universidad Autónoma de Puebla, Puebla, Pue 72570, Mexico; Instituto de Ciencias Básicas e Ingeniería, Universidad Autónoma del Estado de Hidalgo, Mineral de la Reforma, Hidalgo 42184, Mexico; orcid.org/0000-0001-6713-9160

Francisco Enrique Cancino-Gordillo – Instituto de Física, Benemérita Universidad Autónoma de Puebla, Puebla, Pue 72570, Mexico; orcid.org/0000-0001-8286-5734

Complete contact information is available at: <https://pubs.acs.org/10.1021/acsanm.3c03618>

Notes

The authors declare no competing financial interest.

■ ACKNOWLEDGMENTS

The authors thank CONAHCyT, Mexico, for the financial support through the project CB-A1-S-26720. Ortiz-Quiñonez thanks CONAHCyT, Mexico, for providing postdoctoral fellowship. Cancino-Gordillo thanks CONAHCyT, Mexico, for the doctoral fellowship.

■ REFERENCES

- (1) Chromium in drinking-water. Background document for development of WHO Guidelines for drinking-water quality. <https://apps.who.int/iris/bitstream/handle/10665/338062/WHO-HEP-ECH-WSH-2020.3-eng.pdf?sequence=1&isAllowed=y> (accessed Jul 28, 2023).
- (2) Apte, A. D.; Tare, V.; Bose, P. Extent of Oxidation of Cr(III) to Cr(VI) under Various Conditions Pertaining to Natural Environment. *J. Hazard. Mater.* **2006**, *128*, 164–174.
- (3) Liang, J.; Huang, X.; Yan, J.; Li, Y.; Zhao, Z.; Liu, Y.; Ye, J.; Wei, Y. A Review of the Formation of Cr(VI) via Cr(III) Oxidation in Soils and Groundwater. *Sci. Total Environ.* **2021**, *774*, 145762.
- (4) Bai, C.; Wang, L.; Zhu, Z. Adsorption of Cr(III) and Pb(II) by Graphene Oxide/Alginate Hydrogel Membrane: Characterization, Adsorption Kinetics, Isotherm and Thermodynamics Studies. *Int. J. Biol. Macromol.* **2020**, *147*, 898–910.
- (5) Liang, C.; Fu, F.; Tang, B. Mn-Incorporated Ferrihydrite for Cr(VI) Immobilization: Adsorption Behavior and the Fate of Cr(VI) during Aging. *J. Hazard. Mater.* **2021**, *417*, 126073.
- (6) Zhang, W.; Ma, X.; Li, R.; Yang, W.; Li, Q.; Sun, X.; Li, J.; Shen, J. Rapid Sequestration of Chelated Cr(III) by Ferrihydrite: Adsorption and Overall Transformation of Cr(III) Complexes. *Colloids Surf., A* **2021**, *625*, 126819.
- (7) Hexavalent chromium in drinking water. https://portal.ct.gov/-/media/Departments-and-Agencies/DPH/dph/drinking_water/pdf/HexavalentChromiuminDrinkingWaterpdf.pdf (accessed Jul 28, 2023).
- (8) Wang, J.; Mao, M.; Atif, S.; Chen, Y. Adsorption Behavior and Mechanism of Aqueous Cr(III) and Cr(III)-EDTA Chelates on DTPA-Chitosan Modified Fe₃O₄@SiO₂. *React. Funct. Polym.* **2020**, *156*, 104720.
- (9) Unceta, N.; Séby, F.; Malherbe, J.; Donard, O. F. X. Chromium Speciation in Solid Matrices and Regulation: A Review. *Anal. Bioanal. Chem.* **2010**, *397*, 1097–1111.
- (10) Housecroft, C. E.; Sharpe, A. G. *Inorganic Chemistry*, 5th ed.; Pearson Education Limited: Harlow, England, 2018.

- (11) Eyvazi, B.; Jamshidi-Zanjani, A.; Darban, A. K. Synthesis of Nano-Magnetic MnFe_2O_4 to Remove Cr(III) and Cr(VI) from Aqueous Solution: A Comprehensive Study. *Environ. Pollut.* **2020**, *265*, 113685.
- (12) Wu, P.; Zhang, Q.; Dai, Y.; Zhu, N.; Dang, Z.; Li, P.; Wu, J.; Wang, X. Adsorption of Cu(II), Cd(II) and Cr(III) Ions from Aqueous Solutions on Humic Acid Modified Ca-Montmorillonite. *Geoderma* **2011**, *164*, 215–219.
- (13) Wu, H.; Xiao, Y.; Guo, Y.; Miao, S.; Chen, Q.; Chen, Z. Functionalization of SBA-15 Mesoporous Materials with 2-Acetylthiophene for Adsorption of Cr(III) Ions. *Microporous Mesoporous Mater.* **2020**, *292*, 109754.
- (14) Vieira, C. A.; Ferreira, B. F.; Da Silva, A. F.; Vicente, M. A.; Trujillano, R.; Rives, V.; Ciuffi, K. J.; Nassar, E. J.; De Faria, E. H. Adsorption-Based Synthesis of Environmentally Friendly Heterogeneous Chromium(III) Catalysts for Oxidation Reactions into Kaolinite, Saponite, and Their Amine-Modified Derivatives. *ACS Appl. Nano Mater.* **2018**, *1*, 3867–3877.
- (15) Yang, S.; Li, L.; Pei, Z.; Li, C.; Lv, J.; Xie, J.; Wen, B.; Zhang, S. Adsorption Kinetics, Isotherms and Thermodynamics of Cr(III) on Graphene Oxide. *Colloids Surf., A* **2014**, *457*, 100–106.
- (16) Ma, R.; Wang, T.; Huang, T.; Sun, W.; Qiao, S.; Liu, W. Insights into Interactions of Cr(III) and Organic Matters during Adsorption onto Titanate Nanotubes: Differential Absorbance and DFT Study. *J. Mol. Liq.* **2020**, *312*, 113432.
- (17) Zheng, T. R.; Qian, L. L.; Li, M.; Wang, Z. X.; Li, K.; Zhang, Y. Q.; Li, B. L.; Wu, B. A Bifunctional Cationic Metal-Organic Framework Based on Unprecedented Nonanuclear Copper(II) Cluster for High Dichromate and Chromate Trapping and Highly Efficient Photocatalytic Degradation of Organic Dyes under Visible Light Irradiation. *Dalton Trans.* **2018**, *47*, 9103–9113.
- (18) Tadjenant, Y.; Dokhan, N.; Barras, A.; Addad, A.; Jijie, R.; Szunerits, S.; Boukherroub, R. Graphene Oxide Chemically Reduced and Functionalized with KOH-PEI for Efficient Cr(VI) Adsorption and Reduction in Acidic Medium. *Chemosphere* **2020**, *258*, 127316.
- (19) Kong, D.; He, L.; Li, H.; Zhang, F.; Song, Z. Preparation and Characterization of Graphene Oxide/Chitosan Composite Aerogel with High Adsorption Performance for Cr(VI) by a New Crosslinking Route. *Colloids Surf., A* **2021**, *625*, 126832.
- (20) Zheng, Y.; Cheng, B.; You, W.; Yu, J.; Ho, W. 3D Hierarchical Graphene Oxide-NiFe LDH Composite with Enhanced Adsorption Affinity to Congo Red, Methyl Orange and Cr(VI) Ions. *J. Hazard. Mater.* **2019**, *369*, 214–225.
- (21) Liu, W.; Chen, H.; Borthwick, A. G. L.; Han, Y.; Ni, J. Mutual Promotion Mechanism for Adsorption of Coexisting Cr(III) and Cr(VI) onto Titanate Nanotubes. *Chem. Eng. J.* **2013**, *232*, 228–236.
- (22) Krishna Kumar, A. S.; Jiang, S. J.; Warchol, J. K. Synthesis and Characterization of Two-Dimensional Transition Metal Dichalcogenide Magnetic $\text{MoS}_2@Fe_3O_4$ Nanoparticles for Adsorption of Cr(VI)/Cr(III). *ACS Omega* **2017**, *2*, 6187–6200.
- (23) Paris, E. C.; Malafatti, J. O. D.; Musetti, H. C.; Manzoli, A.; Zenatti, A.; Escote, M. T. Faujasite Zeolite Decorated with Cobalt Ferrite Nanoparticles for Improving Removal and Reuse in Pb^{2+} Ions Adsorption. *Chin. J. Chem. Eng.* **2020**, *28*, 1884–1890.
- (24) Klekotka, U.; Wińska, E.; Zambrycka-Szelewa, E.; Satula, D.; Kalska-Szostko, B. Magnetic Nanoparticles as Effective Heavy Ion Adsorbers in Natural Samples. *Sensors* **2022**, *22*, 3297.
- (25) Ederer, J.; Janoš, P.; Ecorchard, P.; Tolasz, J.; Štengl, V.; Beneš, H.; Perchacz, M.; Pop-Georgievski, O. Determination of Amino Groups on Functionalized Graphene Oxide for Polyurethane Nanomaterials: XPS Quantitation vs Functional Speciation. *RSC Adv.* **2017**, *7*, 12464–12473.
- (26) Kullyakool, S.; Treetong, A.; Soontaranon, S.; Laohhasurayotin, K. Highly Exfoliated Graphene Oxide with Enhanced Carbonyl Content and Facile Amine Functionalization for Biomedical Applications. *ACS Appl. Nano Mater.* **2020**, *3*, 7260–7269.
- (27) Zhang, X.; Zhu, M.; Ouyang, T.; Chen, Y.; Yan, J.; Zhu, K.; Ye, K.; Wang, G.; Cheng, K.; Cao, D. NiFe_2O_4 Nanocubes Anchored on Reduced Graphene Oxide Cryogel to Achieve a 1.8 V Flexible Solid-State Symmetric Supercapacitor. *Chem. Eng. J.* **2019**, *360*, 171–179.
- (28) Marcano, D. C.; Kosynkin, D. V.; Berlin, J. M.; Sinititskii, A.; Sun, Z.; Slesarev, A.; Alemany, L. B.; Lu, W.; Tour, J. M. Improved Synthesis of Graphene Oxide. *ACS Nano* **2010**, *4*, 4806–4814.
- (29) Li, J.; Zhu, J.; Liu, X. Ultrafine Silver Nanoparticles Obtained from Ethylene Glycol at Room Temperature: Catalyzed by Tungstate Ions. *Dalton Trans.* **2014**, *43*, 132–137.
- (30) Smith, R. M.; Martell, A. E. *Critical Stability Constants*; Springer: New York, 1977 DOI: 10.1007/978-1-4613-4452-0.
- (31) Breternitz, J. *A Contribution toward the Performance and Structural Understanding of Copper and Nickel Salts as Ammonia Stores*; Doctoral dissertation, Glasgow University, 2016.
- (32) Zhu, M.; Meng, D.; Wang, C.; Diao, G. Facile Fabrication of Hierarchically Porous CuFe_2O_4 Nanospheres with Enhanced Capacitance Property. *ACS Appl. Mater. Interfaces* **2013**, *5*, 6030–6037.
- (33) Biesinger, M. C. Accessing the Robustness of Adventitious Carbon for Charge Referencing (Correction) Purposes in XPS Analysis: Insights from a Multi-User Facility Data Review. *Appl. Surf. Sci.* **2022**, *597*, 153681.
- (34) Samson, V. A.; Bernadsha, S. B.; Xavier, R.; Rueshwin, C. S. T.; Prathap, S.; Madhavan, J.; Raj, M. V. A. One Pot Hydrothermal Synthesis and Characterization of NiFe_2O_4 Nanoparticles. *Mater. Today: Proc.* **2022**, *50*, 2665–2667.
- (35) Ortiz-Quinonez, J. L.; Das, S.; Pal, U. Catalytic and Pseudocapacitive Energy Storage Performance of Metal (Co, Ni, Cu and Mn) Ferrite Nanostructures and Nanocomposites. *Prog. Mater. Sci.* **2022**, *130*, 100995.
- (36) Iraqui, S.; Kashyap, S. S.; Rashid, M. H. NiFe_2O_4 Nanoparticles: An Efficient and Reusable Catalyst for the Selective Oxidation of Benzyl Alcohol to Benzaldehyde under Mild Conditions. *Nanoscale Adv.* **2020**, *2*, 5790–5802.
- (37) Cai, Y. Z.; Cao, W. Q.; Zhang, Y. L.; He, P.; Shu, J. C.; Cao, M. S. Tailoring RGO- NiFe_2O_4 Hybrids to Tune Transport of Electrons and Ions for Supercapacitor Electrodes. *J. Alloys Compd.* **2019**, *811*, 152011.
- (38) Sawai, O.; Zhou, X.; Yoko, A.; Hirai, D.; Nunoura, T. Organic Solvent-Free Process for the Rapid Fabrication of Nickel Ferrite-Reduced Graphene Oxide as a Magnetic Nanosorbent Using Supercritical Water. *Ind. Eng. Chem. Res.* **2021**, *60*, 9897–9905.
- (39) Liang, J.; Wei, Y.; Zhang, J.; Yao, Y.; He, G.; Tang, B.; Chen, H. Scalable Green Method to Fabricate Magnetically Separable NiFe_2O_4 -Reduced Graphene Oxide Nanocomposites with Enhanced Photocatalytic Performance Driven by Visible Light. *Ind. Eng. Chem. Res.* **2018**, *57*, 4311–4319.
- (40) Ren, F.; Zhu, G.; Ren, P.; Wang, K.; Cui, X.; Yan, X. Cyanate Ester Resin Filled with Graphene Nanosheets and CoFe_2O_4 -Reduced Graphene Oxide Nanohybrids as a Microwave Absorber. *Appl. Surf. Sci.* **2015**, *351*, 40–47.
- (41) Yin, W.; Hao, S.; Cao, H. Solvothermal Synthesis of Magnetic CoFe_2O_4 /RGO Nanocomposites for Highly Efficient Dye Removal in Wastewater. *RSC Adv.* **2017**, *7*, 4062–4069.
- (42) Kalita, C.; Boruah, P. K.; Das, M. R.; Saikia, P. Facile Green Synthesis of Nickel-Ferrite-RGO (NiFe_2O_4 /RGO) Nanocomposites for Efficient Water Purification under Direct Sunlight. *Inorg. Chem. Commun.* **2022**, *146*, 110073.
- (43) Boychuk, V.; Zapukhlyak, R.; Hodlevsky, M.; Kotsyubynsky, V.; Turovska, L. Surfactant-Assisted Hydrothermal Synthesis of NiFe_2O_4 /Reduced Graphene Oxide Composites. *Mater. Today Proc.* **2022**, *62*, 5705–5711.
- (44) Wang, G.; Ma, Y.; Mu, J.; Zhang, Z.; Zhang, X.; Zhang, L.; Che, H.; Bai, Y.; Hou, J.; Xie, H. Monodisperse Polyvinylpyrrolidone-Coated CoFe_2O_4 Nanoparticles: Synthesis, Characterization and Cytotoxicity Study. *Appl. Surf. Sci.* **2016**, *365*, 114–119.
- (45) Zhang, H. J.; Liu, L. Z.; Zhang, X. R.; Zhang, S.; Meng, F. N. Microwave-Assisted Solvothermal Synthesis of Shape-Controlled CoFe_2O_4 Nanoparticles for Acetone Sensor. *J. Alloys Compd.* **2019**, *788*, 1103–1112.

- (46) Medina, M. A.; Oza, G.; Ángeles-Pascual, A.; González, M.; Antaño-López, R.; Vera, A.; Leija, L.; Reguera, E.; Arriaga, L. G.; Hernández Hernández, J. M.; Ramírez, J. T. Hyperthermia of Monodispersed Cobalt Ferrite Nanoparticles for Cancer Therapeutics. *Molecules* **2020**, *25*, 4428.
- (47) Xu, S.; Ma, Y.; Geng, B.; Sun, X.; Wang, M. The Remanence Ratio in CoFe_2O_4 Nanoparticles with Approximate Single-Domain Sizes. *Nanoscale Res. Lett.* **2016**, *11*, 471.
- (48) Kumar, Y.; Shirage, P. M. Highest Coercivity and Considerable Saturation Magnetization of CoFe_2O_4 Nanoparticles with Tunable Band Gap Prepared by Thermal Decomposition Approach. *J. Mater. Sci.* **2017**, *52*, 4840–4851.
- (49) Simon, C.; Zakaria, M. B.; Kurz, H.; Tetzlaff, D.; Blösser, A.; Weiss, M.; Timm, J.; Weber, B.; Apfel, U.; Marschall, R. Magnetic NiFe_2O_4 Nanoparticles Prepared via Non-Aqueous Microwave-Assisted Synthesis for Application in Electrocatalytic Water Oxidation. *Chem. – Eur. J.* **2021**, *27*, 16990–17001.
- (50) De Wijs, G. A.; Fang, C. M.; Kresse, G.; De With, G. First-Principles Calculation of the Phonon Spectrum of MgAl_2O_4 Spinel. *Phys. Rev. B* **2002**, *65*, No. 094305.
- (51) Chandramohan, P.; Srinivasan, M. P.; Velmurugan, S.; Narasimhan, S. V. Cation Distribution and Particle Size Effect on Raman Spectrum of CoFe_2O_4 . *J. Solid State Chem.* **2011**, *184*, 89–96.
- (52) Ferrari, A. C. Raman Spectroscopy of Graphene and Graphite: Disorder, Electron-Phonon Coupling, Doping and Nonadiabatic Effects. *Solid State Commun.* **2007**, *143*, 47–57.
- (53) De Silva, K. K. H.; Viswanath, P.; Rao, V. K.; Suzuki, S.; Yoshimura, M. New Insight into the Characterization of Graphene Oxide and Reduced Graphene Oxide Monolayer Flakes on Si-Based Substrates by Optical Microscopy and Raman Spectroscopy. *J. Phys. Chem. C* **2021**, *125*, 7791–7798.
- (54) Ferrari, A. C.; Basko, D. M. Raman Spectroscopy as a Versatile Tool for Studying the Properties of Graphene. *Nat. Nanotechnol.* **2013**, *8*, 235–246.
- (55) Dresselhaus, M. S.; Jorio, A.; Souza Filho, A. G.; Saito, R. Defect Characterization in Graphene and Carbon Nanotubes Using Raman Spectroscopy. *Philos. Trans. R. Soc., A* **2010**, *368*, 5355–5377.
- (56) Jiao, X.; Qiu, Y.; Zhang, L.; Zhang, X. Comparison of the Characteristic Properties of Reduced Graphene Oxides Synthesized from Natural Graphites with Different Graphitization Degrees. *RSC Adv.* **2017**, *7*, 52337–52344.
- (57) Larkin, P. J. *Infrared and Raman Spectroscopy: Principles and Spectral Interpretation*, 1st ed.; Elsevier: Waltham, MA, USA, 2011.
- (58) Moulder, J. F.; Stickle, W. F.; Sobol, P. F.; Kenneth, B. D. *Handbook of X-Ray Photoelectron Spectroscopy*, 1st ed.; Perkin-Elmer Corporation: Eden Prairie, 1992.
- (59) Rabchinskii, M. K.; Ryzhkov, S. A.; Kirilenko, D. A.; Ulin, N. V.; Baidakova, M. V.; Shnitov, V. V.; Pavlov, S. L.; Chumakov, R. G.; Stolyarova, D. Y.; Besedina, N. A.; Shvidchenko, A. V.; Potorochin, D. V.; Roth, F.; Smirnov, D. A.; Gudkov, M. V.; Brzhezinskaya, M.; Lebedev, O. L.; Melnikov, V. P.; Brunkov, P. N. From Graphene Oxide towards Aminated Graphene: Facile Synthesis, Its Structure and Electronic Properties. *Sci. Rep.* **2020**, *10*, 6902.
- (60) Li, X.; Wang, H.; Robinson, J. T.; Sanchez, H.; Diankov, G.; Dai, H. Simultaneous Nitrogen Doping and Reduction of Graphene Oxide. *J. Am. Chem. Soc.* **2009**, *131*, 15939–15944.
- (61) Jiang, L.; Xu, G.; Fu, Y. Catalytic Cleavage of the C-O Bond in Lignin and Lignin-Derived Aryl Ethers over $\text{Ni}/\text{AlP}_x\text{O}_x$ Catalysts. *ACS Catal.* **2022**, *12*, 9473–9485.
- (62) Sing, K. S. W.; Everett, D. H.; Haul, R. A. W.; Moscou, L.; Pierotti, R. A.; Rouquérol, J.; Siemieniewska, T. Reporting Physisorption Data for Gas/Solid Systems with Special Reference to the Determination of Surface Area and Porosity. *Int. Union Pure Appl. Chem.* **1985**, *57*, 603–619.
- (63) Kosmulski, M. Compilation of PZC and IEP of Sparingly Soluble Metal Oxides and Hydroxides from Literature. *Adv. Colloid Interface Sci.* **2009**, *152*, 14–25.
- (64) Bhosale, S. V.; Suryawanshi, S. R.; Bhoraskar, S. V.; More, M. A.; Joag, D. S.; Mathe, V. L. Influence of Morphology and Crystallinity on Field Emission Properties of NiFe_2O_4 Nanoparticles Grown by High-Temperature Vapor Phase Condensation Route. *Mater. Res. Express* **2015**, *2*, 95001.
- (65) Sukumar, M.; Rajabathar, J. R.; AL-Lohedan, H.; Suresh, S.; Dash, C. S.; Sundararajan, M.; Subudhi, P. S.; Arokiyaraj, S.; Yanmaz, E.; Yuvaraj, S.; Isaac, R. S. R. Synthesize and Characterization of Copper Doped Nickel Ferrite Nanoparticles Effect on Magnetic Properties and Visible Light Catalysis for Rhodamine Dye Degradation Mechanism. *J. Alloys Compd.* **2023**, *953*, 169902.
- (66) Liu, W.; Yu, Y. Ultrafast Advanced Treatment of Chromium Complex-Containing Wastewater Using Co/Fe Layered Double Hydroxide. *Environ. Technol. Innov.* **2022**, *26*, 102296.
- (67) Ho, Y. S.; McKay, G. A Comparison of Chemisorption Kinetic Models Applied to Pollutant Removal on Various Sorbents. *Process Saf. Environ. Prot.* **1998**, *76*, 332–340.
- (68) Ranasinghe, S. H.; Navaratne, A. N.; Priyantha, N. Enhancement of Adsorption Characteristics of Cr(III) and Ni(II) by Surface Modification of Jackfruit Peel Biosorbent. *J. Environ. Chem. Eng.* **2018**, *6*, 5670–5682.
- (69) Pal, U.; Sandoval, A.; Madrid, S. I. U.; Corro, G.; Sharma, V.; Mohanty, P. Mixed Titanium, Silicon, and Aluminum Oxide Nanostructures as Novel Adsorbent for Removal of Rhodamine 6G and Methylene Blue as Cationic Dyes from Aqueous Solution. *Chemosphere* **2016**, *163*, 142–152.
- (70) Anamika; Singh, V.; Yadav, B. K. Adsorption Study of Heavy Metals from Aqueous Solutions Using Magnetite Nanoparticles. *J. Phys. Conf. Ser.* **2020**, *1504*, 012011.